

DTIC FILE COPY

Naval Research Laboratory

Washington, DC 20375-5000



NRL Memorandum Report 6299

AD-A200 348

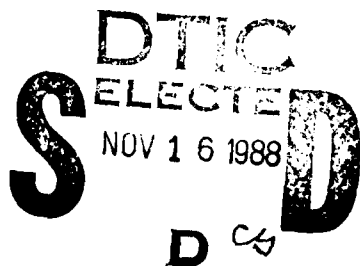
The Theory of Final Focusing of Intense Light Ion Beams

J. J. WATROUS

*National Research Council
Naval Research Laboratory
Research Associate*

P. F. OTTINGER AND D. MOSHER

*Plasma Technology Branch
Plasma Physics Division*



October 26, 1988

88 11 15 063

Approved for public release; distribution unlimited

SECURITY CLASSIFICATION OF THIS PAGE

REPORT DOCUMENTATION PAGE				Form Approved OMB No 0704-0188	
1a REPORT SECURITY CLASSIFICATION UNCLASSIFIED			1b RESTRICTIVE MARKINGS		
2a SECURITY CLASSIFICATION AUTHORITY			3 DISTRIBUTION/AVAILABILITY OF REPORT		
2b DECLASSIFICATION/DOWNGRADING SCHEDULE			Approved for public release; distribution unlimited.		
4 PERFORMING ORGANIZATION REPORT NUMBER(S) NRL Memorandum Report 6299			5 MONITORING ORGANIZATION REPORT NUMBER(S)		
6a NAME OF PERFORMING ORGANIZATION Naval Research Laboratory		6b OFFICE SYMBOL (If applicable) Code 4770		7a NAME OF MONITORING ORGANIZATION	
6c ADDRESS (City, State, and ZIP Code) Washington, DC 20375-5000			7b ADDRESS (City, State, and ZIP Code)		
8a NAME OF FUNDING/SPONSORING ORGANIZATION Department of Energy		8b OFFICE SYMBOL (If applicable)		9 PROCUREMENT INSTRUMENT IDENTIFICATION NUMBER	
8c ADDRESS (City, State, and ZIP Code) Washington, DC 20545			10 SOURCE OF FUNDING NUMBERS		
			PROGRAM ELEMENT NO	PROJECT NO	TASK NO 08-79 DP40092
			WORK UNIT ACCESSION NO DN680-382		
11 TITLE (Include Security Classification) The Theory of Final Focusing of Intense Light Ion Beams					
12 PERSONAL AUTHOR(S) Watrous, * J., Ottinger, P.F. and Mosher, D.					
13a TYPE OF REPORT Interim		13b TIME COVERED FROM _____ TO _____		14 DATE OF REPORT (Year, Month, Day) 1988 October 26	
15 PAGE COUNT 87					
16 SUPPLEMENTARY NOTATION This is an expanded version of the article submitted to the Physics of Fluids for publication & contains more details of the calculations than the Physics of Fluids publication. *National Research Council/Naval Research Laboratory Associate					
17 COSATI CODES			18 SUBJECT TERMS (Continue on reverse if necessary and identify by block number)		
FIELD	GROUP	SUB-GROUP	Ion beams; Final focusing; Inertial confinement fusion; Transport channels. (15)		
19 ABSTRACT (Continue on reverse if necessary and identify by block number) <p>Efficient transport of the high power light ion beams of interest to inertial confinement fusion experiments may require the use of large radius transport channels. The mismatch in the radii of the transported ion beam and the ICF target requires that the beam be focused following large radius transport. A theoretical description of intense light ion beam focusing with a z-discharge plasma is presented. The theory is based on a Vlasov equation description of a fully charge and current neutralized ion beam, neglecting any angular momentum of the beam ions. An initial ion beam phase space distribution with adjustable parameters is considered so that its effect upon the phase space distribution at the focal plane can be analyzed. A numerical code is used to analyze the effect of angular momentum on the focusing properties of the final focusing cell. The theoretical analysis indicates that the proposed focusing method is viable. The numerical analysis indicates that even if beam ions have a significant amount of angular momentum, the beam can still be focused as indicated by the zero angular momentum theory.</p>					
20 DISTRIBUTION/AVAILABILITY OF ABSTRACT <input checked="" type="checkbox"/> UNCLASSIFIED/UNLIMITED <input type="checkbox"/> SAME AS RPT <input type="checkbox"/> DTIC USERS			21 ABSTRACT SECURITY CLASSIFICATION UNCLASSIFIED		
22a NAME OF RESPONSIBLE INDIVIDUAL P.F. Ottinger			22b TELEPHONE (Include Area Code) (202) 767-2610 Code 4771		

DD Form 1473, JUN 86

S/N 0102-LF-014-6603

CONTENTS

I.	INTRODUCTION	1
II.	REQUIREMENTS ON SYSTEM PARAMETERS	3
III.	VLASOV EQUATION ANALYSIS OF Z-DISCHARGE TRANSPORT AND FOCUSING	7
	A. Solution of the Vlasov Equation	8
	B. Treatment of the Transport Channel	14
	C. Treatment of the Final Focusing Cell	21
	D. Treatment of the Ballistic Drift Region	25
IV.	NUMERICAL TREATMENT OF Z-DISCHARGE TRANSPORT AND FOCUSING	32
V.	DISCUSSION OF RESULTS	38
	ACKNOWLEDGEMENTS	41
	APPENDIX	43
	REFERENCES	50
	DISTRIBUTION LIST	85



A-1

THE THEORY OF FINAL FOCUSING OF INTENSE LIGHT ION BEAMS

I. INTRODUCTION

Light ion beam inertial confinement fusion experiments on PBFA II at Sandia National Laboratories currently employ barrel-shaped applied-B ion diodes¹. In diodes of this type, the ion beam is created on the inner surface of the barrel, and is focused on its centerline². Barrel geometry diodes will be unsuitable for future high gain target experiments because target explosions will irradiate the surrounding structure, producing unacceptably high levels of radioactivity. High gain target experiments will require that PBFA II be reconfigured to provide isolation by moving the target several meters from the diode region of the accelerator. The currently envisioned reconfiguration, called APEX, employs an ion diode in the extractor geometry focusing the beam into an ion transport channel that guides the beam to the target^{3,4}.

Channel transport is a technique for transporting an intense ion beam over a distance of several meters⁵. The ion beam is focused on the entrance of a long z-discharge transport channel. If the density of the channel plasma is sufficiently high, the beam can propagate in a fully charge and current neutralized mode^{6,7}. In addition, the z-discharge current creates an azimuthal magnetic field that can confine the propagating beam ions to the path of the discharge⁸. An intense ion beam can travel through a z-discharge transport channel for distances of several meters without significant energy loss⁹. Channel transport is important to the APEX project for two reasons. First, it provides an efficient way of getting the ion beam from the diode to a target located several meters away. Second, channel transport over such distances allows the ion beam to be axially compressed by time-of-flight bunching. This time-of-flight bunching, produced by a carefully programmed accelerator voltage waveform, provides the ion beam power levels and pulse widths required for high gain target experiments¹⁰.

Several issues involved with channel transport have been considered previously. Experimentally, the concept has been tested and verified for relatively low power proton beams^{9,11,12,13}. Ion beam propagation in channels and the MHD response of the channel plasma to the ion beam have been studied theoretically^{8,14,15,16}. Electrostatic and electromagnetic instabilities have also been studied theoretically^{17,18,19,20}. Many of the theoretical issues have been summarized in terms of constraints on the beam transport channel system for optimal beam transport²¹. APEX severely tests these constraints because of the high ion beam power required at the target - on the order of 300 TW. The beam is injected at a lower power level and axially compressed by time-of-flight bunching so that system parameters must satisfy the transport constraints over the entire length of the channel with varying beam power and pulse duration taken into account. A detailed examination of this issue has indicated that the transport constraints can be satisfied if the channel radius is sufficiently large. For example, channel expansion and beam energy loss considerations both show that transportable beam power scales with the fourth power of the channel radius^{10,15}. For the parameters of interest to the APEX project, the smallest radius that allows all of the relevant constraints to be consistently satisfied is between 2 and 3 cm. However, currently envisioned high gain targets are typically less than 1 cm in radius. A solution to the mismatch between the target radius and the beam radius is to focus the beam onto the target following transport. The final focusing cell must compress the beam radially by a factor of three to five.

A method for producing the required radial compression using a short z-discharge plasma at the end of the transport channel has been proposed²². This method relies on the radial oscillations induced in the ion beam envelope by a sudden change in the strength of the azimuthal magnetic field. When the beam enters a region of increased magnetic field strength, the radial oscillations begin with an inward

pinch. A z-discharge channel can be used to focus an ion beam if its length is such that at the exit, the beam is in the pinching phase of the envelope oscillation. The beam then comes to a focus at a position downstream from the focusing cell exit. In this paper the focusing of an intense ion beam with a short z-discharge is analyzed theoretically. Section II will describe the basic system requirements for ion beam transport. Section III will examine the final focusing technique with a Vlasov equation analysis. This analysis is restricted to a highly idealized model of the transport channel, focusing cell, and ion beam. A simulation code has been developed that allows ion beam propagation and focusing to be studied in less ideal situations. In Section IV, this code is used to analyze the impact of angular momentum on final focusing. Section V summarizes the theoretical and numerical analysis of final focusing, and indicates the directions of ongoing and future research in this area.

II. Requirements on System Parameters

The essential physics of intense ion beam transport in a z-discharge channel can be understood from a single particle description. This fortunate circumstance is due to the assumption that the ion beam propagates in a fully charge and current neutralized mode. Under that assumption, each beam ion experiences only the force of the azimuthal magnetic field produced by the discharge current.

The basic components of the ion beam production, transport, and focusing system are illustrated in Figure 1. Ions are produced and accelerated in the ion diode. The voltage pulse produced by the pulsed power generator accelerates the ions to energies in the range of tens of MeV. The ion beam is focused by a combination of geometric focusing produced by shaping both the anode surface and the cathode foil and by

its self magnetic field in the anode-cathode gap. After passing through the cathode foil, the ion beam enters a neutral gas region where it is rapidly charge and current neutralized. In this region, the ions focus ballistically onto the channel entrance. The angle with which an ion enters the transport channel can be estimated from the geometry of the ion diode. If F is the focal length of the diode, and R is the maximum radius at which ions are produced in the diode, then the maximum angle at which an ion enters the channel is

$$\alpha_0 = R / F. \quad (1)$$

The spotsize produced at the diode focal plane is determined by the microdivergence, a measure of the spread in radial velocities produced by nonideal effects in the diode. Letting $\Delta\theta$ denote the microdivergence in radians, the spotsize is given by

$$r_s = F \Delta\theta. \quad (2)$$

Equations (1) and (2) determine the initial conditions, $\alpha = \alpha_0$ and $r = r_s$, for that ion which is the most difficult to confine in the transport channel. In Eq. (1), it is assumed that the microdivergence angle $\Delta\theta$ is much less than the geometric focusing angle R/F .

The motion of an ion in the transport channel is characterized by a betatron orbit. An ion propagating through the channel experiences a radial restoring force due to the radial component of $\mathbf{v} \times \mathbf{B}$. As a result, the ion undergoes a radial oscillation as it travels down the transport channel. In a magnetic field consisting of only an axially uniform azimuthal component, the motion of an ion is characterized by three constants of the motion. They are the kinetic energy, the canonical axial momentum, and the canonical angular momentum:

$$v^2 = v_r^2 + v_z^2 + v_\theta^2 = \text{constant}, \quad (3a)$$

$$P_z = mv_z - \frac{q}{c} \int B_\theta(r) dr = \text{constant}, \quad (3b)$$

$$P_\theta = mrv_\theta = \text{constant}, \quad (3c)$$

where cgs-es units are used throughout. These three constants of the motion may be used to derive an expression that relates the radial position and the radial velocity of an ion to the discharge current. For the case of an ion with zero angular momentum ($P_\theta = 0$), a magnetic field of the form

$$B_\theta(r) = \frac{2I_c}{cr_c} \frac{r}{r_c}, \quad (4)$$

and with a small axis crossing angle, this expression takes the form

$$r^2 + \left(\frac{\lambda_{\beta 0}}{2\pi} \right)^2 \alpha^2 = r_{tp}, \quad (5)$$

where

$$\lambda_{\beta 0} = 2\pi r_c \sqrt{\frac{mc^2 v}{2qI_c}}, \quad (6)$$

$\alpha = v_r/v$ and r_{tp} is the radial turning point. Eq. (5) shows that under the assumptions noted above, the trajectory of an ion in the radial phase space plane is an ellipse. This expression may also be derived as the first integral of the radial equation of motion. The quantity $\lambda_{\beta 0}$ is the betatron wavelength, and is the axial distance required for an ion to complete one full trip around the radial phase space ellipse. Because all ions have the same betatron wavelength under this approximation, the radial phase space distribution of the propagating beam is a periodic function of the propagation distance. The initial distribution reappears at intervals equal to the betatron wavelength. The terms neglected in Eq. (5) under the small axis-crossing angle approximation cause ions with different radial turning points to have slightly different betatron wavelengths. This results in phase mixing that gradually washes out the dependence of the radial phase space distribution on the propagation distance. This is discussed in more detail in the next section. A relation analogous to Eq. (5) exists for the more general case of nonzero angular momentum, large axis-crossing angles, and more general radial distributions of the azimuthal magnetic field, but the radial phase space trajectory is then no longer an ellipse.

The combination of the constants of the motion expressed by Eq. (5) is significant because it relates the production and focusing of the ion beam to the transport of the beam in the discharge channel. In particular, Eq. (5) can be used to find the minimum value of the discharge current required to produce an azimuthal magnetic field that is sufficiently strong to confine all the beam ions to the transport channel given the parameters which characterize how the beam is injected into the channel. Setting r_{tp} in Eq. (5) to r_c , the channel radius, and setting $r = r_s$ and $\alpha = R/F$ (Eqs. (1) and (2)), and solving Eq. (5) for the discharge current gives

$$I_c = \frac{mc^2 v}{2q} \frac{(R/F)^2}{1 - r_s^2/r_c^2} \quad (7)$$

For example, consider injecting 30 MeV Li_7^{+3} ions into a 3 cm radius transport channel with $r_s = r_c/2^{1/2}$. Suppose that a beam current of 1 MA is required, and that the extraction ion diode has a source density of 10 kA/cm² with a microdivergence of 20 mrad. To produce the required ion beam current of 1 MA, the anode must have a surface area of 100 cm². Thus, the anode radius must be about 5.7 cm. From Eq. (2), the focal length required to focus to a spotsize of 2.121 cm from an extraction diode with a 20 mrad microdivergence is about 106 cm. Thus, (R/F) has a value of 0.0535, and Eq. (7) indicates that the transport channel discharge current must be about 20 kA. For the analysis presented below, a value of $I_c = 20$ kA is chosen for the numerical simulations, but it should be noted that the values of the parameters discussed here are important primarily when considering transport and focusing in relation to the rest of the beam production system.

III. Vlasov Equation Analysis of Z-Discharge Transport and Focusing

The single-particle analysis of the preceding section illustrated some of the basic ideas of intense ion beam transport. In this section, a Vlasov equation analysis will be employed to describe both transport and focusing. Because of the assumption of complete charge and current neutralization, the Vlasov equation can be decoupled from Maxwell's equations, which would otherwise need to be solved simultaneously to describe the self-consistent fields. Previous analysis of this problem⁸ is extended here to treat the final focusing cell and the ballistic drift zone between the focusing cell exit and the focal plane. The first

subsection describes the Vlasov equation analysis. The following three subsections apply the analysis to the propagation of the ion beam in the transport channel, the final focusing cell, and the ballistic drift region, respectively. The areal number density of the ion beam at the focal plane, as well as expressions for the spotsize and focal length of the focusing cell will be obtained.

A. Solution of the Vlasov Equation

Several other assumptions will be made in addition to the assumption of complete charge and current neutralization. It will be assumed that the transport channel parameters can be chosen to minimize the hydrodynamic response of the channel to the passage of the beam as well as to provide an acceptably small collisional beam energy loss during propagation^{21,23}. This assumption has a number of helpful consequences. First, it means that on the time scale that characterizes the ion beam duration, the channel can be treated as a time independent configuration. Second, the axial electric field induced by the hydrodynamic interaction of the neutralizing return current with the discharge magnetic field¹⁵ can be considered to be negligible. In addition to this induced electric field, there is an axial electric field associated with the resistive flow of the neutralizing current. However, for Spitzer resistivity the force produced by this electric field on a beam ion is three orders of magnitude or more smaller than the $v \times B$ force experienced by a beam ion in the discharge magnetic field. Thus, both the resistive and the inductive parts of the axial electric field can be neglected. This, in conjunction with the assumption of small collisional beam energy loss, means that the energy of the propagating beam ions can be approximated as constant. It will also be assumed that the beam is free from elastic scattering collisions that would lead to a diffusion of the beam in velocity space. The above assumptions allow the beam to be regarded as a collection of noninteracting ions propagating through the static

azimuthal magnetic field of the z-discharge transport channel. The evolution of the ion beam phase space distribution can be described by the Vlasov equation. To simplify that equation to the point where analytic progress can be made, three more assumptions will be made. First, the discharge current density is assumed to be uniform inside the channel radius, r_c , and zero at greater radii. The azimuthal magnetic field corresponding to this current density distribution then has a linear radial profile inside the channel, as given by Eq. (4). Second, all beam ions are assumed to have zero angular momentum. Third, the investigation will be limited to a beam produced by a monoenergetic time-independent source, so that time-of-flight effects are neglected. Under the assumptions stated, the Vlasov equation describing the phase space distribution of the ion beam is

$$v_r \frac{\partial f}{\partial r} + v_z \frac{\partial f}{\partial z} + \left(\frac{2qI_c}{mcr_c^2} \right) r \left[v_r \frac{\partial f}{\partial v_z} - v_z \frac{\partial f}{\partial v_r} \right] = 0. \quad (8)$$

Since the solution to the Vlasov equation is a function of the equations of motion, one could immediately use the constants of the motion discussed in Section II to develop a solution. However, because of the particular form of the initial radial phase space distribution to be considered here, it is more convenient to solve Eq. (8) using the method of characteristics. Eq. (8) will be rearranged by using the conservation of energy to reduce the number of independent variables. Letting α denote the pitch angle of an ion trajectory, and letting v denote the magnitude the velocity of a beam ion, the radial and axial velocity components can be written as

$$v_r = v \sin \alpha, \quad (9a)$$

$$v_z = v \cos \alpha, \quad (9b)$$

and the Vlasov equation takes the form

$$v \sin \alpha \frac{\partial f}{\partial r} + v \cos \alpha \frac{\partial f}{\partial z} - \left(\frac{2q I_c}{mc r_c^2} \right) r \frac{\partial f}{\partial \alpha} = 0. \quad (10)$$

This equation is posed as an initial value problem by specifying the distribution in the plane $z = 0$, corresponding to the entrance of the transport channel. The distribution function for $z > 0$ is then obtained by solving Eq. (10) using the method of characteristics.

The characteristic equations associated with Eq. (10) are

$$\frac{dr}{d\tau} = v_b \sin \alpha \quad \text{with} \quad r(0) = r_0, \quad (11a)$$

$$\frac{dz}{d\tau} = v_b \cos \alpha \quad \text{with} \quad z(0) = z_0, \quad (11b)$$

$$\frac{d\alpha}{d\tau} = - \left(\frac{2q I_c}{mc r_c^2} \right) r \quad \text{with} \quad \alpha(0) = \alpha_0, \quad (11c)$$

$$\text{and} \quad \frac{df}{d\tau} = 0 \quad \text{with} \quad f(0) = F(r_0, \alpha_0, z_0). \quad (11d)$$

In this analysis the initial ion beam phase space distribution will be defined at a plane $z_0 = 0$. Thus, $\tau = 0$ corresponds to $z_0 = 0$ and the parameter z_0 will be suppressed in the following analysis. Equation (10) is solved by solving Eqs. (11a), (11b), (11c), and (11d), inverting these solutions to obtain r_0 and α_0 as functions of r , z , and α , and inserting those expressions into $F(r_0, \alpha_0)$. By differentiating Eq. (11c) with respect to τ , and using Eq. (11a) to eliminate $dr/d\tau$, the pendulum equation is obtained for $\alpha(\tau)$:

$$\frac{d^2\alpha}{d\tau^2} + \omega_{\beta 0}^2 \sin \alpha = 0, \quad (12)$$

$$\text{where at } \tau = 0, \quad \begin{cases} \alpha = \alpha_0, \\ \frac{d\alpha}{d\tau} = - \frac{\omega_{\beta 0}^2 r_0}{v_b}, \end{cases}$$

and where $\omega_{\beta 0}$ is defined by

$$\omega_{\beta 0}^2 = \frac{2q I_c}{mc r_c^2} v_b \quad (13)$$

Equation (12) may be solved exactly in terms of Jacobian elliptic functions, however, a solution in terms of these functions makes the next step, inverting for r_0 and α_0 , very difficult. To avoid this difficulty, Eq. (12) is linearized using the small angle approximation, namely $\sin(\alpha) \approx \alpha$. This approximation is justified since the strength of the azimuthal magnetic field typically considered for the transport channel is sufficiently strong to confine only those ions with small axis-crossing angles. While the use of more intense magnetic fields would certainly allow ions with larger axis-crossing angles to be confined, there are other reasons concerning the energetics of driving a long, high current discharge and the evolution and stability of the discharge that make lower field strengths preferable. In the linearized version of Eq. (12), $\omega_{\beta 0}$ is the radial frequency of oscillations and is termed the betatron frequency. The solution to the linearized version of Eq. (12) is

$$\alpha(\tau) = - \frac{[r_0^2 + (\lambda_{\beta 0} \alpha_0 / 2\pi)^2]^{1/2}}{\lambda_{\beta 0} / 2\pi} \sin \left[\omega_{\beta 0} \tau - \tan^{-1} \left(\frac{\alpha_0 \lambda_{\beta 0}}{2\pi r_0} \right) \right] \quad (14)$$

In the small angle approximation, the betatron wavelength $\lambda_{\beta 0}$ is related to the betatron frequency by

$$\lambda_{\beta 0} = 2\pi v_b / \omega_{\beta 0}. \quad (15)$$

Equation (14) and the corresponding solution to Eq. (11a) may be inverted to obtain

$$r_0 = r \cos(\omega_{\beta 0} \tau) - (\lambda_{\beta 0} / 2\pi) \alpha \sin(\omega_{\beta 0} \tau), \quad (16)$$

$$\alpha_0 = (2\pi / \lambda_{\beta 0}) r \sin(\omega_{\beta 0} \tau) + \alpha \cos(\omega_{\beta 0} \tau). \quad (17)$$

The linearization that allowed Eq. (12) to be solved so easily is equivalent to approximating the axial component of the velocity of a beam ion by the constant v_b . Thus, the parameter τ can be replaced by $z/v_z = z/v_b$. This gives

$$r_0(r, z, \alpha) = r \cos(k_\beta z) - (\alpha/k_\beta) \sin(k_\beta z), \quad (18a)$$

$$\alpha_0(r, z, \alpha) = (r/k_\beta) \sin(k_\beta z) + \alpha \cos(k_\beta z), \quad (18b)$$

where $k_\beta = 2\pi/\lambda_{\beta 0}$. The solution to the Vlasov equation can then be written as

$$f(r, \alpha, z) = F(r_0(r, \alpha, z), \alpha_0(r, \alpha, z)) \quad (19)$$

It remains only to specify the initial distribution $F_0(r_0, \alpha_0)$.

B. Treatment of the Transport Channel

In the original analysis of intense light ion beam propagation in z-discharge transport channels⁸, the initial distribution filled a rectangle in radial phase space centered about $r = 0$ and $v_r = 0$ such that at $z = 0$, the number density profile was $n(r) = \text{constant}$ for $r < r_s$ and $n(r) = 0$ for $r > r_s$. In this analysis, the initial radial phase space distribution will be generalized to include rectangles in the radial phase space plane with arbitrary boundaries. The reason for extending this analysis to more general initial distributions is to find what impact the form of the initial distribution has on the focused ion beam number density profile. The initial distributions considered here are simple models of what would be produced by an extraction ion diode at or near its focal plane. Figure 2 illustrates this initial condition which can be expressed mathematically as

$$\begin{aligned}
F(r_{ot}, \alpha_{ot}) = & N \delta(v_{\theta ot}) \frac{1}{v_{ot}} \delta(v_{ot} - v_b) \\
& \left[H(r_{ot} - r_{min}) - H(r_{ot} - r_{max}) \right] \times \\
& \left(\left[H(\alpha_{ot} - \alpha_{min}) - H(\alpha_{ot} - \alpha_{max}) \right] + \right. \\
& \left. \left[H(\alpha_{ot} + \alpha_{max}) - H(\alpha_{ot} + \alpha_{min}) \right] \right), \quad (20)
\end{aligned}$$

where H is the Heaviside step function ($H(x) = 0$ for $x < 0$, $H(x) = 1$ for $x > 0$). The subscript "ot" denotes the initial condition for propagation in the transport channel. The delta functions are included to specify that the beam is monoenergetic and has no angular momentum. The quantity v is the magnitude of the velocity of an ion and v_b is the specific value of the magnitude of the velocity of the beam ions. N is the average density of this initial distribution and for this particular distribution is given by $N_0 / [(\alpha_{max} - \alpha_{min})\pi(r_{max}^2 - r_{min}^2)]$, where N_0 is the total number of ions present at the source plane $z = 0$. Note that by integrating this distribution over the velocity space coordinates, the resulting radial number density profile is flat between r_{min} and r_{max} and is zero elsewhere.

The downstream phase space density is obtained by using Eqs. (18a) and (18b) to express r_{ot} and α_{ot} in Eq. (20) in terms of r , α , and z . The delta function in $v_{\theta ot}$ is transformed to $(r/r_{ot})\delta(v_\theta)$ using the conservation of angular momentum and the delta function relation $\delta(ax) = \delta(x)/|a|$. Similarly, the conservation of energy allows the quantity v to be replaced by v_b . The result is a phase space density that is periodic in z . This purely periodic behavior is a consequence of the

small angle linearization used to solve Eq. (13), which gave all beam ions the same betatron frequency, $\lambda_{\beta 0}$. By forgoing this approximation and solving the equations of motion exactly, one finds that the actual betatron wavelength of an ion depends on the turning point. The equations of motion may be posed in either the time domain, in order to find the betatron frequency, or in the axial distance domain, in order to find the betatron wavelength. From the calculation in the axial distance domain, the exact result for the betatron wavelength is

$$\lambda_{\beta}(r_{tp}) = \frac{2}{\pi} \lambda_{\beta 0} \left[2E\left(\pi \frac{r_{tp}}{\lambda_{\beta 0}}\right) - K\left(\pi \frac{r_{tp}}{\lambda_{\beta 0}}\right) \right] \quad (22)$$

$$= \lambda_{\beta 0} \left[1 - \frac{3\pi^2}{4} \left(\frac{r_{tp}}{\lambda_{\beta 0}} \right)^2 \right] \quad (23)$$

where K and E are the complete elliptic integrals of the first kind and second kinds, respectively. Eq. (23) is an approximate result obtained from the small argument expansions of the complete elliptic integrals that is valid when the channel radius is much smaller than the betatron wavelength. The result indicates that if the initial distribution has a finite spread in either r_{0t} or α_{0t} , there will be a corresponding spread in the betatron wavelengths of the propagating ions. This spread will manifest itself as a phase mixing of the downstream distribution. For a beam with ions which cross the axis with small angles, i.e. a low emittance beam, a propagation distance of many betatron wavelengths is

required for phase mixing to be complete⁸, where complete phase mixing implies that the radial phase space distribution of the beam becomes independent of z . It will be assumed here that the transport channel is long enough to allow complete phase mixing to occur. Rather than dealing explicitly with the problem of phase mixing, an approximate phase mixed distribution will be obtained by averaging the periodic distribution over the betatron wavelength $\lambda_{\beta 0}$:

$$f^{\text{pm}}(r, \alpha) = \frac{1}{\lambda_{\beta 0}} \int_z^{\lambda_{\beta 0} + z} dz' f(r, \alpha, z'). \quad (24)$$

Specifically,

$$f^{pm} = \frac{N}{\pi} \frac{\rho}{r} \delta(v_{\theta}) \frac{\delta(v - v_b)}{v} \times \quad (25)$$

$$\int_{-1}^1 dx \left(\left[H\left(\sqrt{1-x^2} - \frac{r_{\min}}{\rho}\right) - H\left(\sqrt{1-x^2} - \frac{r_{\max}}{\rho}\right) \right] \times \right. \\ \left. \left[H\left(x + \frac{\alpha_{\max}}{k_{\beta}\rho}\right) - H\left(x + \frac{\alpha_{\min}}{k_{\beta}\rho}\right) \right] + \right. \\ \left. \left[H\left(x - \frac{\alpha_{\min}}{k_{\beta}\rho}\right) - H\left(x - \frac{\alpha_{\max}}{k_{\beta}\rho}\right) \right] \right) ,$$

where $\rho^2 = r^2 + \alpha^2 / k_{\beta}^2$.

To complete the integration, one must specify the relative magnitudes of α_{\min} , α_{\max} , r_{\min} , and r_{\max} . To do so, it is convenient to express the combination $(\lambda_{\beta 0} \alpha) / 2\pi$ as a new variable γ . In the r - γ phase space plane, the phase space trajectory of a propagating beam ion is a circle rather than an ellipse. There are then two results, depending on the magnitude of $(\gamma_{\max}^2 + r_{\min}^2)^{1/2}$ relative to $(r_{\max}^2 + \gamma_{\min}^2)^{1/2}$. The two results correspond to two different orientations of the rectangle that defines the initial radial phase space distribution as illustrated in Figures 3a and 3b. For $\gamma_{\max}^2 + r_{\min}^2 < r_{\max}^2 + \gamma_{\min}^2$, that rectangle is oriented horizontally, and the ion beam phase mixed distribution is

$$f^{pm} = \frac{2N}{\pi r} \delta(v_\theta) \frac{\delta(v - v_b)}{v} \left\{ \begin{array}{ll} 0; & \rho^2 < r_{\min}^2 + \gamma_{\min}^2 \\ \sqrt{\rho^2 - r_{\min}^2} - \gamma_{\min}; & r_{\min}^2 + \gamma_{\min}^2 < \rho^2 \\ \gamma_{\max} - \gamma_{\min}; & \rho^2 < r_{\min}^2 + \gamma_{\max}^2 \\ \gamma_{\max} - \sqrt{\rho^2 - r_{\max}^2}; & r_{\min}^2 + \gamma_{\max}^2 < \rho^2 \\ 0; & \rho^2 < r_{\max}^2 + \gamma_{\min}^2 \\ & r_{\max}^2 + \gamma_{\min}^2 < \rho^2 \\ & \rho^2 < r_{\max}^2 + \gamma_{\max}^2 \\ & r_{\max}^2 + \gamma_{\max}^2 < \rho^2 \\ & \rho^2 < r_{\max}^2 + \gamma_{\max}^2 \\ & \rho^2 > r_{\max}^2 + \gamma_{\max}^2 \end{array} \right. \quad (26)$$

For $\gamma_{\max}^2 + r_{\min}^2 > r_{\max}^2 + \gamma_{\min}^2$, the initial phase space distribution rectangle is oriented vertically, and the ion beam phase mixed distribtuion is

$$f^{pm} = \frac{2N}{\pi r} \delta(v_\theta) \frac{\delta(v - v_b)}{v} \left\{ \begin{array}{ll} 0; & \rho^2 < r_{\min}^2 + \gamma_{\min}^2 \\ \sqrt{\rho^2 - r_{\min}^2} - \gamma_{\min}; & r_{\min}^2 + \gamma_{\min}^2 < \rho^2 \\ \sqrt{\rho^2 - r_{\min}^2} - \sqrt{\rho^2 - r_{\max}^2}; & \rho^2 < r_{\max}^2 + \gamma_{\min}^2 \\ \gamma_{\max} - \sqrt{\rho^2 - r_{\max}^2}; & r_{\max}^2 + \gamma_{\min}^2 < \rho^2 \\ 0; & \rho^2 < \gamma_{\max}^2 + r_{\min}^2 \\ & \gamma_{\max}^2 + r_{\min}^2 < \rho^2 \\ & \rho^2 < r_{\max}^2 + \gamma_{\max}^2 \\ & \rho^2 > r_{\max}^2 + \gamma_{\max}^2 \end{array} \right. \quad (27)$$

Although somewhat complex in appearance, these results have a simple geometric interpretation. After phase mixing, the radial phase space distribution is a function of ρ modulated by a factor of $1/r$. The $1/r$ modulation is a consequence of the cylindrical geometry. The dependence on ρ reflects the fact that in the r - γ plane, ions move on circles defined by $r^2 + \gamma^2 = \rho^2 = \text{constant}$. The intensity of the phase mixed distribution on any given circle is proportional to the average value of r on the portion of that circle that lies within the region defined by the initial radial phase space distribution. The phase mixed distribution functions represent the state of the ion beam after many

betatron wavelengths of propagation in the transport channel, and will be used as the initial condition for describing beam propagation in the final focusing cell.

C. Treatment of the Final Focusing Cell

The final focusing cell will be described by an idealized model similar to that used for the transport channel - a uniform cylindrical plasma carrying a uniformly distributed discharge current within radius r_c . For the present, the exact length of the final focusing cell will not be specified. However, its length need not be greater than a quarter betatron wavelength to take advantage of the envelope oscillations. In the final focusing cell, the beam clearly does not propagate far enough to phase mix and, in fact, the z -dependence of the beam distribution function is the central issue. The analysis of beam focusing will determine the optimal final focusing cell length.

The phase space density of the ion beam in the final focusing cell is obtained by propagating the phase mixed distribution (either Eq. (26) or Eq. (27)) along the trajectories of ions. The characteristic equations that describe the ion trajectories for the focusing cell are the same as for the transport channel (Eqs. (11a) and (11b)) except for the difference in the magnetic field strength. Since the phase mixed distribution is being used as an initial condition for propagation in the final focusing cell, the quantity ρ in either of Eqs. (26, or (27) must be interpreted as a function of the initial phase space coordinates. Thus, $\rho^2 = r_{of}^2 + \alpha_{of}^2/k_\beta^2$, where the subscript "of" denotes the initial conditions for propagation in the final focusing cell. With the modifications appropriate to the increase in the magnetic field strength, Eqs. (18a) and (18b) may be used for expressing ρ in terms of the downstream radial phase space coordinates. Letting I_f denote the

discharge current in the final focusing cell and introducing the parameters

$$\Delta = \frac{I_f}{I_c} - 1, \quad (28)$$

$$\Omega_{\beta 0}^2 = \left(\frac{v_b}{r_c} \right) \left(\frac{2q I_f}{mc^2 r_c} \right), \quad \text{and} \quad (29)$$

$$\Lambda_{\beta 0} = \left(\frac{v_b}{2\pi\Omega_{\beta 0}} \right), \quad (30)$$

the combination of r_{of} and α_{of} denoted by ρ in Eqs. (26) and (27) may be expressed as

$$\begin{aligned} \rho^2 &= r_{of}^2 + \alpha_{of}^2 / k_{\beta}^2 \\ &= r^2 + \alpha^2 / K_{\beta}^2 + \Delta [r \sin(K_{\beta} z) + (\alpha / K_{\beta}) \cos(K_{\beta} z)], \quad (31) \end{aligned}$$

where Γ and K_{β} for the final focusing cell are defined analogously to γ and k_{β} for the transport channel, namely, $K_{\beta} = 2\pi/\Lambda_{\beta 0}$ and $\Gamma = \alpha/K_{\beta}$. This expression for ρ is inserted into Eqs. (26) and (27) to give the ion beam phase space distribution in the final focusing cell.

The phase space distributions obtained in this manner depend on r and Γ only through the combination which defines ρ . The equation $\rho^2 = \text{constant}$ defines an ellipse in the r - Γ plane which rotates as the beam moves through the final focusing cell. To examine this result in further detail, it is useful to use a coordinate system which rotates relative to the original coordinate system in such a manner that in the new coordinate system, the phase space ellipse does not rotate. The equation for the ellipse may be written as

$$A r^2 + B r\Gamma + C \Gamma^2 = \rho^2, \quad (32)$$

$$\text{where } A = 1 + \Delta \sin^2(K_\beta z), \quad (33)$$

$$B = 2\Delta \sin(K_\beta z) \cos(K_\beta z), \text{ and} \quad (34)$$

$$C = 1 + \Delta \cos^2(K_\beta z). \quad (35)$$

The constant ρ in this equation denotes any of the boundaries in r - Γ space at which the functional form of the phase mixed phase space distribution changes. For example, in Eq. (26), the phase space distribution function is zero for $\rho^2 \leq r_{\min}^2 + (\lambda_{\beta 0}/2\pi)^2 \alpha_{\min}^2$ but attains a different functional form for $\rho^2 > r_{\min}^2 + (\lambda_{\beta 0}/2\pi)^2 \alpha_{\min}^2$. In this case,

$p = r_{\min}^2 + (\lambda_{\beta 0}/2\pi)^2 \alpha_{\min}^2$. The new rotating coordinate frame is defined by the relations

$$r = r' \cos\psi - \Gamma' \sin\psi, \quad (36)$$

$$\Gamma = r' \sin\psi + \Gamma' \cos\psi. \quad (37)$$

The proper choice of the angle ψ will eliminate the cross term in the rotating frame, reducing the equation for the ellipse to normal form. The proper choice is

$$\psi = (1/2) \cot^{-1} [(A - C)/B] = -2\pi z/\lambda_{\beta 0}. \quad (38)$$

In the new rotating frame, the equation for the ellipse is

$$(r')^2 / p^2 + (\Gamma')^2 / [p^2/(1 + \Delta)] = 1. \quad (39)$$

This indicates that the phase space distribution is characterized by concentric ellipses which, in the original nonrotating frame, rotate in the clockwise sense such that the angle between their major axes and the r -axis is $2\pi z/\lambda_{\beta 0}$ radians.

Figures 4a and 4b show how the radial phase space distribution has changed after propagating one quarter and one-eighth of a betatron wavelength through the focusing cell, respectively. If the beam is allowed to propagate a quarter of a betatron wavelength into the cell, the phase space ellipse will rotate by -90° so its major axis is parallel to the Γ -axis. At this point, the radius of the beam is determined by the minor axis of the phase space ellipse:

$$r_{\text{foc}} = \sqrt{\frac{I_c}{I_f + I_c}} r_c \quad (40)$$

This could be useful for focusing, but it would require the that target be placed immediately at the exit of the final focusing cell. A more practical approach would allow for standoff between the final focusing cell exit and the target. The best way of accomplishing this is to use a one-eighth betatron wavelength long focusing cell. This creates a radial phase space distribution at the focusing cell exit in which the number of ions with negative radial velocities is maximized. The ion beam then comes to a focus as it ballistically propagates through the standoff region. For the remainder of this analysis, only the one-eighth betatron wavelength focusing method will be considered.

D. Treatment of the Ballistic Drift Region

The propagation of the ion beam in field free space may be described, once again, by the Vlasov equation. In this case, however, the discharge current appearing the Eq. (10) is absent; the ions follow straight line

trajectories. The solution and inversion of the characteristic equations is trivial:

$$r_{ob} = r - \alpha z, \quad (41a)$$

$$\alpha_{ob} = \alpha, \quad (41b)$$

where the subscript "ob" denotes the initial values for propagation in the ballistic drift region. The ion beam phase space distribution in the ballistic drift region is obtained by using Eqs. (41a) and (41b) to propagate the phase space distribution at the final focusing cell exit along the ballistic ion trajectories. At the exit of the final focusing cell, the quantity ρ must be interpreted as a function of the initial conditions for ballistic propagation. From Eq. (31) and using $z = \Lambda_{\beta 0}/8$, at the final focusing cell exit ρ is given by

$$\rho^2 = r_{ob}^2 + (\alpha_{ob}/K_{\beta})^2 + \frac{\Delta}{2} (r_{ob} + \alpha_{ob}/K_{\beta})^2. \quad (42a)$$

coordinates in terms of the downstream coordinates gives

$$\rho^2 = \frac{1}{2} \left[(2 + \Delta) r^2 + 2(\Delta/K_{\beta} - (2 + \Delta)z) \alpha r + \left((2 + \Delta)z^2 + (2 + \Delta)/K_{\beta}^2 - 2\Delta z/K_{\beta} \right) \alpha^2 \right]. \quad (42b)$$

Using this as the definition for ρ is Eqs. (26) and (27) then gives the ion beam phase space distribution in field free space.

It is again useful to write the equation for the ellipse that characterizes the phase space distribution in normal form. Proceeding as before, the equation for the phase space ellipse can be written as

$$\frac{\left(\frac{1}{2}(2 + \Delta) + [\Delta - (2 + \Delta)Z]\cos\xi\sin\xi - \frac{1}{2}Z[2\Delta - (2 + \Delta)Z]\sin^2\xi\right)}{p^2} r, 2 +$$

$$\frac{\left(\frac{1}{2}(2 + \Delta) - [\Delta - (2 + \Delta)Z]\cos\xi\sin\xi - \frac{1}{2}Z[2\Delta - (2 + \Delta)Z]\cos^2\xi\right)}{p^2} r, 2$$

$$= 1, \quad (43)$$

where the angle ξ between the rotating and stationary axes is now given by

$$\xi = -\frac{1}{2} \tan^{-1} \left[\frac{2}{Z} \left(\frac{\Delta - (2 + \Delta)Z}{2\Delta - (2 + \Delta)Z} \right) \right], \quad (44)$$

where $Z = 2\pi z/\lambda_{\beta 0}$. This analysis indicates that in the coordinate frame in which the equation for the phase space ellipse appears in normal form, the phase space ellipse undergoes an area preserving deformation characterized by a decrease in the length of the major axis and a corresponding increase in the length of the minor axis, as illustrated in Figure 5. At $Z = \Delta/(2 + \Delta)$ the lengths of the major and minor axes are equal. For greater values of Z , the roles of the major and minor axes are reversed, with the original major axis becoming the minor axis as the ellipse grows progressively more eccentric along what was originally the minor axis. The rotating coordinate frame, which at the exit of the final focusing cell was oriented with its r' -axis making an angle of -45° to the r -axis, begins to rotate counterclockwise. At $Z = \Delta/(2 + \Delta)$, the rotating frame has rotated back to 0° with respect to the r -axis. At $Z = 2\Delta/(2 + \Delta)$, it has rotated to $+45^\circ$. Downstream from that point, the direction of rotation reverses and asymptotically approaches 0° as Z approaches infinity. It should be emphasized that what is actually rotating is the coordinate frame defined by the major and minor axes of the ellipse. The actual ions move along lines of $\alpha = \text{constant}$ with r increasing with z .

The smallest radius of the ballistically propagating beam is achieved at $Z = \Delta/(2 + \Delta)$, i.e. at a distance of $2\pi\lambda_{\beta 0} \Delta/(2 + \Delta)$ downstream from the exit of the final focusing cell. At that point the ion beam radius is

$$r_{\text{foc}} = \sqrt{\frac{2I_c}{I_f + I_c}} r_c . \quad (45)$$

Note that this is a factor of $2^{1/2}$ greater than could be achieved with a quarter betatron wavelength focusing cell, but that it does provide a standoff of $2\pi\lambda_{\beta 0} \Delta / (2 + \Delta)$ between the final focusing cell exit and the focal plane.

The number density profile of the ion beam at the focal plane is a quantity of central interest to target design since it is that quantity which determines energy deposition profiles. The number density $n(r, z)$ of the ion beam can be obtained from the phase space distribution by integrating over velocity coordinates:

$$n(r, z) = \int dv_{\theta} d\alpha v dv f(r, z, v_{\theta}, v, \alpha) \quad (46)$$

The integrations involved with obtaining $n(r, z)$ from the phase space distribution given in Eqs. (26) and (27), although elementary, are quite lengthy. The results are summarized in the Appendix where the complete expressions for the beam number density profile at the focal plane are given. Due to the complicated functional form of these results, it is convenient to evaluate $n(r)$ for several specific cases to help illustrate the nature of the results. In Figure 6a, $rn(r)$ is shown for the beam at the entrance to the final focusing cell and at the focal plane for the case of the distribution given by Eq. (17). In this example,

$r_{\max} = 2.121$ cm, $\alpha_{\max} = 0.0535$ radians, $r_{\min} = 0$ cm, and $\alpha_{\min} = 0.025$ radians. The comparison of the unfocused beam number density profile to the focused beam number density profile clearly illustrates the ability of the final focusing cell to focus the beam. Figure 6b shows $rn(r)$ for the beam at the focal plane for three different

values of α_{\min} with r_{\max} , α_{\max} , and r_{\min} the same as in Figure 6a. As in Figure 6a, these results correspond to the distribution given by Eq. (17). Figure 7 shows results analogous to those in Figure 6a, but for the distribution given by Eq. (18). In Figure 7, $r_{\max} = 2.121$ cm, $\alpha_{\max} = 0.0535$ radians, $\alpha_{\min} = 0$ radians, and r_{\min} takes on several different values as indicated. In Figs. 6a, 6b, and 7 the transport channel current was 20 kA, the final focusing cell current was 340 kA, the channel radius was 3 cm, and the beam consisted of 30 MeV ${}^3_7\text{Li}$ ions. The quantities r_{\max} and α_{\max} must be constrained to insure that ions injected into the transport channel are confined by the transport channel magnetic field, i.e. Eq. (5) must be satisfied for $r = r_{\max}$, $\alpha = \alpha_{\max}$, and $r_{\text{tp}} = r_c$. The choices of r_{\max} and α_{\max} used in Figs. 5a, 5b, and 6 correspond to $r_{\max}^2 = (\alpha_{\max}/k_\beta)^2 = r_c^2/2$.

The results exhibit several common features. In all cases, the number density is singular at $r = 0$. This singularity is due to the cylindrical geometry, which requires that the volume density of ions diverge at the axis if there are a finite number of ions located there, and to phase mixing, which insures that there are always ions located on the axis. Second, the radius of the ion beam at the focal plane is given by Eq. (45). This indicates, for example, that to produce a factor of two radial compression, the ratio of focusing cell current to transport channel current must be 7. For very large current ratios, the ratio of focused beam radius to channel radius is approximately $(2I_c/I_f)^{1/2}$. In any case, the beam compression ratio depends only on the ratio of the currents. Third, depending on the values of r_{\min} and α_{\min} , the number density profile exhibits an off-axis peak that occurs just inside the radius

$$r_{\text{peak}} = \sqrt{\frac{2}{2 + \Delta} (r_{\min}^2 + \alpha_{\max}^2/k_\beta^2)} \quad (47)$$

for the beam characterized by the distribution given by Eq. (26) and

$$r_{\text{peak}} \approx \sqrt{\frac{2}{2 + \Delta} (r_{\text{max}}^2 + \alpha_{\text{min}}^2 / k_{\beta}^2)} \quad (48)$$

for the beam characterized by the distribution given by Eq. (27). These off-axis peaks are a consequence of the hole in the radial phase space distribution of the phase mixed beam in these examples. When there are no ions in the center of the elliptical radial phase space distribution, the projection of that distribution onto the r-axis is somewhat depressed around $r = 0$. The examples show that the larger the hole in the center of the radial phase space ellipse is, the more dramatic the off-axis peak is.

IV. NUMERICAL TREATMENT OF Z-DISCHARGE TRANSPORT AND FOCUSING

The Vlasov equation analysis of the preceding section treats the restricted case of zero-angular momentum ions propagating in a z-discharge plasma with a uniformly distributed discharge current. Analysis of less restrictive cases, in which the restriction on angular momentum is relaxed, are interesting for a variety of reasons. For example, the applied-B ion diode operates with magnetic fields that can impart angular momentum to the ions it accelerates. Both pinch reflex ion diodes and applied-B diodes suffer from microdivergence which can produce a small level of angular momentum in the accelerated ions. The impact of this effect on the focused beam number density profile may be important to target design. To address these issues, a numerical treatment has been used.

In the original analysis⁸ of z-discharge transport and focusing, a computer code was used to augment the analysis. A computer code of the same type has been developed for the present analysis. The code computes the trajectories of an arbitrary number of ions with arbitrary initial conditions moving in an arbitrary magnetic field. By properly specifying the initial conditions and the magnetic field structure, the code simulates the propagation of an ion beam in a transport channel or final focusing cell. As with the analysis of the previous section, this numerical treatment is based on the assumptions that the beam is fully charge and current neutralized and that the propagation medium is static. In its current usage the code is time-independent in the same sense as was the Vlasov equation treatment; while the trajectory of an individual ion is computed as a function of time, time-independence in the code is achieved by propagating a collection of ions from one plane $z = z_0$ to a downstream plane $z = z_1$ without regard to the time-of-flight of the ions. The main operation of the code is quite simple. It reads a file containing the phase space coordinates of N ions, computes their trajectories in a specified magnetic field, and, when all N ions have

arrived at the collection plane, it writes their phase space coordinates to a new file. An auxiliary code reads this file to perform diagnostics.

As a demonstration of the performance of the code, a run has been performed that simulates the case of zero angular momentum ions shown in Figure 6a. This was the case of zero angular momentum 30 MeV ${}^3_7\text{Li}$ ions injected into a 20 kA, 3 cm radius channel. The maximum and minimum injection angles were 0.0535 and 0 radians, respectively. The maximum and minimum injection radii were 2.121 and 0.0 cm, respectively. 5100 ions were used for this example.

Rather than to propagate this distribution through the many betatron wavelengths that would be required for phase mixing, a phase mixed distribution was obtained using an averaging procedure analogous to that used in the Vlasov equation analysis. The resulting distribution is illustrated in Figure 8a, where the radial phase space positions of all 5100 particles are plotted. The averaging process "smeared-out" the initial distribution over the phase space trajectories of the ions, producing a distribution that, aside from the effect of using a finite number of particles, is independent of the angle in the radial phase space plane. Figure 8b shows the $rn(r)$ profile (number density profile time radius) of this distribution. In these plots, $rn(r)$ is shown rather than $n(r)$ because by multiplying the number density by the radius, the singularity in $n(r)$ at $r = 0$ can be removed, and thereby allow a better comparison between the theoretically predicted result and the simulation result.

This distribution was then propagated through a 340 kA, 3 cm radius one-eighth betatron wavelength final focusing cell. Recall that in this context, the betatron wavelength is determined by discharge current in the focusing cell. For this example, the focusing cell betatron wavelength is 35.22 cm. After exiting the final focusing cell, the beam travelled ballistically to the theoretical location of the focal plane, a

distance of 4.6 cm beyond the focusing cell exit. Figure 9a and 9b show the radial phase space positions and $rn(r)$ profile of the beam at the exit of the final focusing cell. As predicted by the theory, the radial phase space distribution fills an ellipse which has rotated in the clockwise sense. Figures 10a and 10b show the beam radial phase space distribution and radial number density profile at the theoretical focal plane. Fig. 10c shows $rn(r)$ vs r on an expanded scale with the theoretically predicted result overlaid. Aside from the noise due to the use of a finite number of particles, there is very good agreement between the code result and the theoretical prediction.

To assess the impact of angular momentum on final focusing, a code run was performed using the same initial radial phase space distribution used in the theoretical analysis of the preceding section, but with the angular momentum of each ion elevated from zero to the largest value consistent with the requirement that the ion remain confined within the channel. The kinetic energy of each ion was held constant by decreasing v_z as v_θ was increased - because v_θ is much smaller than v_z , the decrease in v_z necessary to keep the same kinetic energy is not great, and does not significantly affect the simulation. The maximum allowable azimuthal velocity can be calculated from the equations of conservation of angular momentum, canonical axial momentum, and energy. These equations can be combined to give

$$\sqrt{v_b^2 - v_r^2 - \frac{r_o^2}{r^2} v_{\theta o}^2} = \sqrt{v_b^2 - v_{ro}^2 - v_{\theta o}^2} + \frac{\omega_c}{2r_{ch}} (r^2 - r_o^2) \quad (49)$$

where ω_c is the cyclotron frequency corresponding to the maximum magnetic field strength, and the subscript "o" denotes the initial conditions for propagation in the transport channel. Requiring that the ion have its outer turning point at $r = r_c$ then yields a quadratic equation for $v_{\theta o}^2$. This equation was used to determine the maximum allowable azimuthal velocity that each ion in the radial phase space distribution could be given. For this simulation, the radial phase space distribution corresponded to curve (a) of Fig. 6b, namely, ions distributed within $0 \leq r \leq 2.121$ cm, $0 < |\alpha| \leq 0.0535$ radians with a flat number density profile. The distribution in r - v_θ is illustrated in Figure 11. Note that this is a highly contrived distribution, but for the given radial phase space distribution, it will show the greatest possible impact that angular momentum can have on final focusing.

An ion with nonzero angular momentum has two turning points as it propagates down the channel. One turning point defines the maximum radial excursion of the ion and the other defines the point of closest approach to the axis. When that inner turning point is very close to the axis, the numerical resolution of the trajectory in that region requires very small timesteps in relation to the timestep size required for accurately resolving the rest of the trajectory. This is so because at the inner turning point, the radially inward $v \times B$ force must balance the radially outward centrifugal force, but since both these quantities are very small when the inner turning point is very close to the axis, large numerical errors occur. In order to avoid extremely restrictive timestep requirements, ions were excluded from the region $0 < r < 0.05$ cm to avoid extremely small points of closest approach. Because of phase mixing, the effect of eliminating the ions in this very narrow strip is negligible. This distribution was then averaged over a betatron wavelength to produce a phase mixed distribution. As in the previous example, the transport channel was a 3 cm radius, 20 kA channel and the ions were 30 MeV ${}^3_7\text{Li}$. The phase mixed distribution was then propagated through a one-eighth

betatron wavelength final focusing cell with a radius of 3 cm and discharge current of 340 kA.

Figures 12a, 12b, and 12c show the $r-v_r$ particle positions, $r-v_\theta$ particle positions, and $rn(r)$ of the phase mixed distribution, i.e. at the entrance to the focusing cell. The radial phase space distribution in this example is notably different from that of the previous no angular momentum example. The finite angular momentum of the ions prevents them from reaching $r = 0$, which modifies the radial phase space distribution by making it very sparse at small radii. Figures 13a, b, and c show the $r-v_r$ and $r-v_\theta$ distributions and the $rn(r)$ profile of the beam at the exit of the final focusing cell. The rotation of the radial phase space distribution that was observed in the previous example is still present, but it is slightly modified at small radii by angular momentum effects. Figures 14 a, b, and c show the $r-v_r$ and $r-v_\theta$ distributions and the $rn(r)$ profile of the beam at the theoretical focal plane. Although there is a large difference in the number density profiles between the zero angular momentum case and this case, there is very little difference in either the spotsizes or the focal lengths. The main effect is a slight increase in the spotsize and a slight decrease in the focal length. This calculation shows that while the highly contrived angular momentum spectrum of the beam has a strong influence over the beam number density profile at the focal plane, the spotsize of the focused beam is not strongly influenced. Thus, the analytic theory of the preceding section should be adequate for predicting the spotsize and focal length of the one-eighth betatron wavelength focusing cell even for beams with appreciable angular momentum.

It should be noted that the dramatic modification of the number density profile of the beam at the focal plane is mainly due to the very contrived angular momentum distribution that was used. That distribution forced the outer turning point of all the ions in the run to be at the channel radius as they propagated in the transport channel, rather than

being distributed between $r = 0$ and $r = r_c$. A more realistic angular momentum spectrum would be expected to have a much less dramatic effect on the radial number density profile of the focused ion beam. This expectation has been confirmed by a simulation of the focusing of a beam that had a spread in azimuthal velocity that was equal to the spread in radial velocity. The initial distribution for this simulation was a uniform distribution of ions within the region $0.05 \text{ cm} \leq r \leq 2.121 \text{ cm}$, $0 \leq |v_r/v_b| \leq 0.0535$, $0 \leq v_\theta/v_b \leq 0.0535$. As in the previous run, ions were excluded from a small region around the axis to avoid numerical difficulties. This initial distribution was phase-averaged in a 20 kA, 3 cm radius transport channel. Figures 15a and 15b show the radial phase space distribution and the v_θ - r distribution of the phase averaged beam. This distribution was then propagated through the same 3 cm, 340 kA one-eighth betatron wavelength focusing cell as was used in the previous example, and was then ballistically propagated to the theoretical focal plane. Figure 16 shows the radial phase space distribution of the focused beam. This figure indicates that the beam is slightly past the focal plane. Figure 17 compares the number density profile of the focused beam obtained from this run with the theoretical number density profile of the corresponding zero angular momentum beam. This comparison indicates that the number density of the beam with angular momentum is different from the zero angular momentum beam mainly at small and intermediate radii. This difference can be ascribed to the difference in the radial phase space trajectories of an ion with zero angular momentum and an ion with finite angular momentum. This difference is greatest at the small radii that cannot be reached by an ion with finite angular momentum. At larger radii, the two profiles are quite similar to one another.

V. Discussion of Results

An analytic treatment of charge and current neutralized ion beam transport and focusing in z-discharge channels has been developed. This treatment has been applied to the one-eighth betatron wavelength focusing method. The theory predicts that beam focusing can be achieved, and that the focused beam radius depends only on $\Delta = I_f/I_c - 1$ and the channel radius, r_c :

$$r_{\text{foc}} = \left(\frac{2}{2 + \Delta} \right)^{1/2} r_c . \quad (50)$$

For the case of an ion beam consisting of zero angular momentum ions, an adjustable initial radial phase space distribution has been used to determine the effect of the initial beam distribution on the beam number density profile at the focal plane. Results indicate that the natural $1/r$ number density profile can be modified to produce an off-axis peak. However, to strongly modify the natural $1/r$ profile requires a very high brightness beam source, i.e. a source with a very small spread in injection angles. A numerical treatment has been used to investigate how nonzero angular momentum effects focusing. A highly contrived distribution, in which all ions had the largest amount of angular momentum possible under the constraint that the ions remain confined in the channel, was used in the code runs. The code runs indicated that while the inclusion of nonzero angular momentum does have a strong effect on the beam number density profile at the focal plane, it does not have a strong effect on either the spotsize or the focal length predicted by the zero angular momentum theory.

The one-eighth betatron wavelength focusing technique provides for a standoff of several centimeters between the exit of the final focusing cell and the focal plane. A one-quarter betatron wavelength focusing cell can focus the beam to a spotsize a factor of $(1/2)^{1/2}$ smaller than a one-eighth betatron wavelength cell for the same ratio of currents, but it does not provide any standoff. Thus, there is a trade-off between the standoff and the radius of the focused beam. Since the targets to be used in the APEX experiments are likely to be cryogenic, the standoff provided by the one-eighth betatron wavelength focusing technique will an important facet of the system design, allowing the target to be isolated from the hot, dense plasma that would be likely to exist in the final focusing cell exit region.

The various portions of the beam production and focusing system are strongly related to one another. The spread in injection angles and radii produced by the extraction diode determine the minimum discharge current, the target radius and the transport channel radius determine the ratio of final focusing cell discharge current to transport channel current, and so on. These relations leave very little freedom in choosing the parameters which define the beam production, transport, and focusing system, and can have a strong impact on the design of the APEX experiment. In fact, by combining Eqs. (45) and (7), a single equation relating all the relevant parameters results:

$$I_f = \left(\frac{2r_c^2 - r_{foc}^2}{r_{foc}^2} \right) \left(\frac{mc^2 v_b}{2q} \right) \left(\frac{(R/F)^2}{1 - (r_s/r_c)^2} \right). \quad (51)$$

The first term in parentheses in Eq. (51) is determined by the transport channel radius and by the target radius. These, in turn, are determined

by the constraints on intense ion beam transport²¹ and by target physics issues, respectively. The second term in parentheses is determined solely by the ion species and energy, which are also determined primarily by target physics issues. The third term in parentheses is determined by the manner in which the ion beam is focused onto the channel entrance from the extraction ion diode, and this involves issues such as the diode microdivergence and source density.

The observation in Part B of Section III concerning the simple geometric interpretation of the phase mixed ion beam phase space distribution opens up the possibility of treating more general initial radial phase space distributions than have been treated here. That observation, namely that the intensity of the phase mixed distribution on any given circle in the r - γ plane is, neglecting the $1/r$ factor, proportional to the value of r averaged over that portion of the circle that passes through the region of initial nonzero radial phase space density, appears to have general validity. It has been confirmed to hold for an initial distribution that filled an arbitrary quadrilateral in the radial phase space plane, and there appears to be no reason that it should not hold for any initial distribution. Thus, the methods used here could be used for analytic treatment of less idealized initial radial phase space distributions. This could have some value when considering specific extraction ion diode designs. Of course, such nonideal distributions can always be treated numerically.

Several features of intense ion beam transport and focusing that have been neglected here will be examined in future investigations. The time dependence of the ion beam source and the beam bunching caused by a carefully programmed accelerator voltage waveform have been neglected here under the assumption of a time-independent source of monoenergetic ions. However, because of the strong effect that the temporal behavior of the beam pulse can have on the performance of a target, it is important to study the time-behavior of the propagating ion beam. In

particular, the dispersion due to the dependence on both the energy and the turning point of the betatron wavelength could have a strong effect on de-bunching an otherwise ideally bunched beam, and could thus be an important feature to consider when designing the accelerator voltage waveform. The reaction of both the transport channel and the final focusing cell to the passage of the ion beam, neglected here under an idealizing assumption, is also a potentially critical issue. The head of the beam could cause a modification in the azimuthal magnetic field profile through a combination of channel expansion and magnetic field convection. This would cause the tail of the beam to travel through a substantially different type of channel and focusing cell than have been assumed here. The difference in the magnetic field profile could affect the time-of-flight bunching through an exaggeration of the effects just mentioned above, as well as degrading the focusing properties of the focusing cell. An analytic investigation of focusing in a one-eighth betatron wavelength cell with a modified magnetic field profile is currently underway, and an investigation of these other effects will follow in the near future.

Acknowledgements

This work was supported by the U.S. Department of Energy through Sandia National Laboratories. One of the authors (JW) was a National Research Council Associate at the Naval Research Laboratory during the time this work was being performed.

Appendix

The beam number density as a function of radius is obtained by integrating the expressions for the beam phase space density, Eqs. (26) or (27), over the velocity space coordinates. For the most part, this amounts to doing integrals of the form

$$\int \sqrt{x^2 \pm a^2} \, dx = \frac{1}{2} \left[x \sqrt{x^2 \pm a^2} \pm a^2 \log \left(x + \sqrt{x^2 \pm a^2} \right) \right]. \quad (A1)$$

For the case of $\gamma_{\max}^2 + r_{\min}^2 < \gamma_{\min}^2 + r_{\max}^2$, corresponding to the phase space distribution given by Eq. 26, the number density profile is:

$$(i) \text{ for } 0 \leq r \leq \left[\frac{2}{2+\Delta} (r_{\min}^2 + \gamma_{\min}^2) \right] \quad (A2)$$

$$\begin{aligned}
 n_b(r) = & \frac{4N}{\Lambda \beta r} \sqrt{\frac{1}{2} \left(\frac{2+\Delta}{2+\Delta} \right)} \times \\
 & \left\{ \frac{\gamma_{\max}}{2} \left[\sqrt{r_{\max}^2 + \gamma_{\max}^2 - \left(\frac{2+\Delta}{2} \right) r^2} - \sqrt{r_{\min}^2 + \gamma_{\max}^2 - \left(\frac{2+\Delta}{2} \right) r^2} \right] \right. \\
 & - \frac{\gamma_{\min}}{2} \left[\sqrt{r_{\max}^2 + \gamma_{\min}^2 - \left(\frac{2+\Delta}{2} \right) r^2} - \sqrt{r_{\min}^2 + \gamma_{\min}^2 - \left(\frac{2+\Delta}{2} \right) r^2} \right] \\
 & - \frac{1}{2} \left[r_{\min}^2 - \left(\frac{2+\Delta}{2} \right) r^2 \right] \log \left[\frac{\gamma_{\max} + \sqrt{r_{\min}^2 + \gamma_{\max}^2 - \left(\frac{2+\Delta}{2} \right) r^2}}{\gamma_{\min} + \sqrt{r_{\max}^2 + \gamma_{\min}^2 - \left(\frac{2+\Delta}{2} \right) r^2}} \right] \\
 & \left. + \frac{1}{2} \left[r_{\max}^2 - \left(\frac{2+\Delta}{2} \right) r^2 \right] \log \left[\frac{\gamma_{\max} + \sqrt{r_{\max}^2 + \gamma_{\max}^2 - \left(\frac{2+\Delta}{2} \right) r^2}}{\gamma_{\min} + \sqrt{r_{\max}^2 + \gamma_{\min}^2 - \left(\frac{2+\Delta}{2} \right) r^2}} \right] \right\}
 \end{aligned}$$

$$(ii) \text{ for } \left[\frac{2}{2+\Delta} (r_{\min}^2 + \gamma_{\min}^2) \right] \leq r \leq \left[\frac{2}{2+\Delta} (r_{\min}^2 + \gamma_{\max}^2) \right] \quad (A3)$$

$$\begin{aligned} n_b(r) = & \frac{4N}{\Lambda_\beta r} \sqrt{\frac{1}{2} \left(\frac{2+\Delta}{2+\Delta} \right)} \times \\ & \left\{ \frac{\gamma_{\max}}{2} \left[\sqrt{r_{\max}^2 + \gamma_{\max}^2 - \left(\frac{2+\Delta}{2} \right) r^2} - \sqrt{r_{\min}^2 + \gamma_{\max}^2 - \left(\frac{2+\Delta}{2} \right) r^2} \right] \right. \\ & - \frac{\gamma_{\min}}{2} \left[\sqrt{r_{\max}^2 + \gamma_{\min}^2 - \left(\frac{2+\Delta}{2} \right) r^2} \right] \\ & - \frac{1}{2} \left[r_{\min}^2 - \left(\frac{2+\Delta}{2} \right) r^2 \right] \log \left[\frac{\gamma_{\max} + \sqrt{r_{\min}^2 + \gamma_{\max}^2 - \left(\frac{2+\Delta}{2} \right) r^2}}{\sqrt{\left(\frac{2+\Delta}{2} \right) r^2 - r_{\min}^2}} \right] \\ & \left. + \frac{1}{2} \left[r_{\max}^2 - \left(\frac{2+\Delta}{2} \right) r^2 \right] \log \left[\frac{\gamma_{\max} + \sqrt{r_{\max}^2 + \gamma_{\max}^2 - \left(\frac{2+\Delta}{2} \right) r^2}}{\gamma_{\min} + \sqrt{r_{\max}^2 + \gamma_{\min}^2 - \left(\frac{2+\Delta}{2} \right) r^2}} \right] \right\} \end{aligned}$$

$$(iii) \text{ for } \left[\frac{2}{2+\Delta} (r_{\min}^2 + \gamma_{\min}^2) \right] \leq r \leq \left[\frac{2}{2+\Delta} (r_{\max}^2 + \gamma_{\min}^2) \right] \quad (A4)$$

$$n_b(r) = \frac{4N}{\Lambda_\beta r} \sqrt{\frac{1}{2} \left(\frac{2+\Delta}{2} \right)} \times$$

$$\left\{ \frac{\gamma_{\max}}{2} \sqrt{r_{\max}^2 + \gamma_{\max}^2 - \left(\frac{2+\Delta}{2} \right) r^2} \right.$$

$$\left. - \frac{\gamma_{\min}}{2} \sqrt{r_{\max}^2 + \gamma_{\min}^2 - \left(\frac{2+\Delta}{2} \right) r^2} \right.$$

$$\left. + \frac{1}{2} \left[r_{\max}^2 - \left(\frac{2+\Delta}{2} \right) r^2 \right] \log \left[\frac{\gamma_{\max} + \sqrt{r_{\max}^2 + \gamma_{\max}^2 - \left(\frac{2+\Delta}{2} \right) r^2}}{\gamma_{\min} + \sqrt{r_{\max}^2 + \gamma_{\min}^2 - \left(\frac{2+\Delta}{2} \right) r^2}} \right] \right\}$$

$$(iv) \text{ for } \left[\frac{2}{2+\Delta} (r_{\min}^2 + \gamma_{\min}^2) \right] \leq r \leq \left[\frac{2}{2+\Delta} (r_{\max}^2 + \gamma_{\max}^2) \right] \quad (A5)$$

$$n_b(r) = \frac{4N}{\Lambda_\beta r} \sqrt{\frac{1}{2} \left(\frac{2+\Delta}{2} \right)} \times$$

$$\left\{ \frac{\gamma_{\max}}{2} \sqrt{r_{\max}^2 + \gamma_{\max}^2 - \left(\frac{2+\Delta}{2} \right) r^2} \right.$$

$$\left. + \frac{1}{2} \left[r_{\max}^2 - \left(\frac{2+\Delta}{2} \right) r^2 \right] \log \left[\frac{\gamma_{\max} + \sqrt{r_{\max}^2 + \gamma_{\max}^2 - \left(\frac{2+\Delta}{2} \right) r^2}}{\sqrt{\left(\frac{2+\Delta}{2} \right) r^2 - r_{\max}^2}} \right] \right\}$$

For the case of $\gamma_{\max}^2 + r_{\min}^2 \geq \gamma_{\min}^2 + r_{\max}^2$, corresponding to the phase space density given by Eq. 27, the number density profile is

$$(i) \text{ for } 0 \leq r \leq \left[\frac{2}{2+\Delta} (r_{\min}^2 + \gamma_{\min}^2) \right] \quad (A6)$$

$$\begin{aligned} n_b(r) = & \frac{4N}{\Lambda_B r} \sqrt{\frac{1}{2} \left(\frac{2+\Delta}{2+\Delta} \right)} \times \\ & \left\{ \frac{\gamma_{\max}}{2} \left[\sqrt{r_{\max}^2 + \gamma_{\max}^2 - \left(\frac{2+\Delta}{2} \right) r^2} - \sqrt{r_{\min}^2 + \gamma_{\max}^2 - \left(\frac{2+\Delta}{2} \right) r^2} \right] \right. \\ & - \frac{\gamma_{\min}}{2} \left[\sqrt{r_{\max}^2 + \gamma_{\min}^2 - \left(\frac{2+\Delta}{2} \right) r^2} - \sqrt{r_{\min}^2 + \gamma_{\min}^2 - \left(\frac{2+\Delta}{2} \right) r^2} \right] \\ & - \frac{1}{2} \left[r_{\min}^2 - \left(\frac{2+\Delta}{2} \right) r^2 \right] \log \left[\frac{\gamma_{\max} + \sqrt{r_{\min}^2 + \gamma_{\max}^2 - \left(\frac{2+\Delta}{2} \right) r^2}}{\gamma_{\min} + \sqrt{r_{\max}^2 + \gamma_{\min}^2 - \left(\frac{2+\Delta}{2} \right) r^2}} \right] \\ & \left. + \frac{1}{2} \left[r_{\max}^2 - \left(\frac{2+\Delta}{2} \right) r^2 \right] \log \left[\frac{\gamma_{\max} + \sqrt{r_{\max}^2 + \gamma_{\max}^2 - \left(\frac{2+\Delta}{2} \right) r^2}}{\gamma_{\min} + \sqrt{r_{\max}^2 + \gamma_{\min}^2 - \left(\frac{2+\Delta}{2} \right) r^2}} \right] \right\} \end{aligned}$$

$$(ii) \text{ for } \left[\frac{2}{2+\Delta} (r_{\min}^2 + \gamma_{\min}^2) \right] \leq r \leq \left[\frac{2}{2+\Delta} (r_{\max}^2 + \gamma_{\min}^2) \right] \quad (A7)$$

$$n_b(r) = \frac{4N}{\Lambda \beta r} \sqrt{\frac{1}{2} \left(\frac{2+\Delta}{2+\Delta} \right)} \times$$

$$\left\{ \begin{aligned} & \frac{\gamma_{\max}}{2} \left[\sqrt{r_{\max}^2 + \gamma_{\max}^2 - \left(\frac{2+\Delta}{2} \right) r^2} - \sqrt{r_{\min}^2 + \gamma_{\max}^2 - \left(\frac{2+\Delta}{2} \right) r^2} \right] \\ & - \frac{\gamma_{\min}}{2} \left[\sqrt{r_{\max}^2 + \gamma_{\min}^2 - \left(\frac{2+\Delta}{2} \right) r^2} \right] \\ & - \frac{1}{2} \left[r_{\min}^2 - \left(\frac{2+\Delta}{2} \right) r^2 \right] \log \left[\frac{\gamma_{\max} + \sqrt{r_{\min}^2 + \gamma_{\max}^2 - \left(\frac{2+\Delta}{2} \right) r^2}}{\sqrt{\left(\frac{2+\Delta}{2} \right) r^2 - r_{\min}^2}} \right] \\ & + \frac{1}{2} \left[r_{\max}^2 - \left(\frac{2+\Delta}{2} \right) r^2 \right] \log \left[\frac{\gamma_{\max} + \sqrt{r_{\max}^2 + \gamma_{\max}^2 - \left(\frac{2+\Delta}{2} \right) r^2}}{\gamma_{\min} + \sqrt{r_{\max}^2 + \gamma_{\min}^2 - \left(\frac{2+\Delta}{2} \right) r^2}} \right] \end{aligned} \right\}$$

$$(iii) \text{ for } \left[\frac{2}{2+\Delta}(r_{\max}^2 + \gamma_{\min}^2) \right] \leq r \leq \left[\frac{2}{2+\Delta}(r_{\min}^2 + \gamma_{\max}^2) \right] \quad (A8)$$

$$n_b(r) = \frac{4N}{\Lambda \beta r} \sqrt{\frac{1}{2} \left(\frac{2+\Delta}{2+\Delta} \right)} \times$$

$$\left\{ \frac{\gamma_{\max}}{2} \left[\sqrt{r_{\max}^2 + \gamma_{\max}^2 - \left(\frac{2+\Delta}{2} \right) r^2} - \sqrt{r_{\min}^2 + \gamma_{\max}^2 - \left(\frac{2+\Delta}{2} \right) r^2} \right] \right.$$

$$- \frac{1}{2} \left[r_{\min}^2 - \left(\frac{2+\Delta}{2} \right) r^2 \right] \log \left[\frac{\gamma_{\max} + \sqrt{r_{\min}^2 + \gamma_{\max}^2 - \left(\frac{2+\Delta}{2} \right) r^2}}{\sqrt{\left(\frac{2+\Delta}{2} \right) r^2 - r_{\min}^2}} \right]$$

$$\left. + \frac{1}{2} \left[r_{\max}^2 - \left(\frac{2+\Delta}{2} \right) r^2 \right] \log \left[\frac{\gamma_{\max} + \sqrt{r_{\max}^2 + \gamma_{\max}^2 - \left(\frac{2+\Delta}{2} \right) r^2}}{\sqrt{\left(\frac{2+\Delta}{2} \right) r^2 - r_{\max}^2}} \right] \right\}$$

$$(iv) \text{ for } \left[\frac{2}{2+\Delta}(r_{\min}^2 + \gamma_{\max}^2) \right] \leq r \leq \left[\frac{2}{2+\Delta}(r_{\max}^2 + \gamma_{\max}^2) \right] \quad (A9)$$

$$n_b(r) = \frac{4N}{\Lambda \beta r} \sqrt{\frac{1}{2} \left(\frac{2+\Delta}{2+\Delta} \right)} \times$$

$$\left\{ \frac{\gamma_{\max}}{2} \sqrt{r_{\max}^2 + \gamma_{\max}^2 - \left(\frac{2+\Delta}{2} \right) r^2} \right.$$

$$\left. + \frac{1}{2} \left[r_{\max}^2 - \left(\frac{2+\Delta}{2} \right) r^2 \right] \log \left[\frac{\gamma_{\max} + \sqrt{r_{\max}^2 + \gamma_{\max}^2 - \left(\frac{2+\Delta}{2} \right) r^2}}{\sqrt{\left(\frac{2+\Delta}{2} \right) r^2 - r_{\max}^2}} \right] \right\}$$

References

- ¹J. P. Vandevender, J. A. Swegle, D. J. Johnson, K. W. Bieg, E. J. T. Burns, J. W. Poukey, P. A. Miller, J. N. Olsen, and G. Yonas, *Laser and Particle Beams*, 3, 93 (1985)
- ²P. L. Dreike, E. J. T. Burns, S. A. Slutz, J. T. Crow, D. J. Johnson, P. R. Johnson, R. J. Leeper, P. A. Miller, L. P. Mix, D. B. Seidel, and D. F. Wenger, *J. Appl. Phys* 60, 878, (1986)
- ³J. P. Van Devender and D. L. Cook, *Science*, 232, 831 (1986)
- ⁴C. L. Olson in Conference Record of the 1987 IEEE International Conference on Plasma Science, (Arlington, VA, 1987) p. 27
- ⁵G. Yonas, *Bull. Am. Phys. Soc.* 21, 1102, (1976)
- ⁶D. A. Hammer and N. Rostoker, *Phys. Fluids* 13, 1831 (1970)
- ⁷D. Mosher and W. W. Hsing, *Bull. Am. Phys. Soc.* 22, 1198 (1977)

- ⁸P. F. Ottinger, D. Mosher, and Shyke A. Goldstein,
Phys. Fluids 23, 909 (1980)
- ⁹F. L. Sandel, F. C. Young, S. J. Stephanakis,
W. F. Oliphant, G. Cooperstein, S. A. Goldstein,
and D. Mosher, Bull. Am. Phys. Soc. 24, 1031 (1979)
- ¹⁰D. Mosher, G. Cooperstein, Shyke A. Goldstein,
D. G. Colombant, P. F. Ottinger, F. L. Sandel,
S. J. Stephanakis, and F. C. Young, in The Proceedings
of the Third International Topical Conference on High
Power Electron and Ion Beam Research and Technology,
(Novosibirsk, USSR, 1979), p. 576
- ¹¹T. Yamada, K. Masugata, K. Yatsui, and M. Matsui,
Japanese J. Appl. Phys. 21, L699 (1982)
- ¹²T. Ozaki, S. Miyamoto, K. Imasaki, S. Nakai, C. Yamamoto,
J. Appl. Phys. 58, 2145 (1985)
- ¹³J. N. Olsen, D. J. Johnson, and R. J. Leeper, Appl. Phys.
Lett. 36, 808 (1980)
- ¹⁴J. R. Freeman, L. Baker, and D. L. Cook. Nuc. Fusion
22, 383 (1982)
- ¹⁵D. G. Colombant, Shyke A. Goldstein, and D. Mosher.

Phys. Rev. Lett., 45, 1253 (1980)

¹⁶A. Mankofsky and R. N. Sudan, Nuc. Fusion, 24, 827 (1984)

¹⁷P. F. Ottinger, D. Mosher, and Shyke A. Goldstein,
Phys. Fluids 22, 332 (1979)

¹⁸P. F. Ottinger, D. Mosher, and Shyke A. Goldstein,
Phys. Fluids 24, 164 (1981)

¹⁹Don S. Lemons, and John R. Cary, J. Appl. Phys. 53, 4093 (1982)

²⁰T. Okada, and K. Niu, J. Phys. Soc. Japan 50, 3845 (1981)

²¹P. F. Ottinger, Shyke A. Goldstein, and D. Mosher, Naval
Research Laboratory Memorandum Report 4948, Nov. 12, 1982

²³P. F. Ottinger, S. A. Goldstein, and D. Mosher.
in Conference Record of the 1980 IEEE International Conference
on Plasma Science. (Madison, WI, 1980). p. 98

²⁴D. Mosher, D. G. Colombant, and Shyke A. Goldstein. Comments
Plasma Physics 6, 101 (1981)

WALL STABILIZED, LIGHT-ION BEAM TRANSPORT AND FINAL FOCUSING SYSTEM

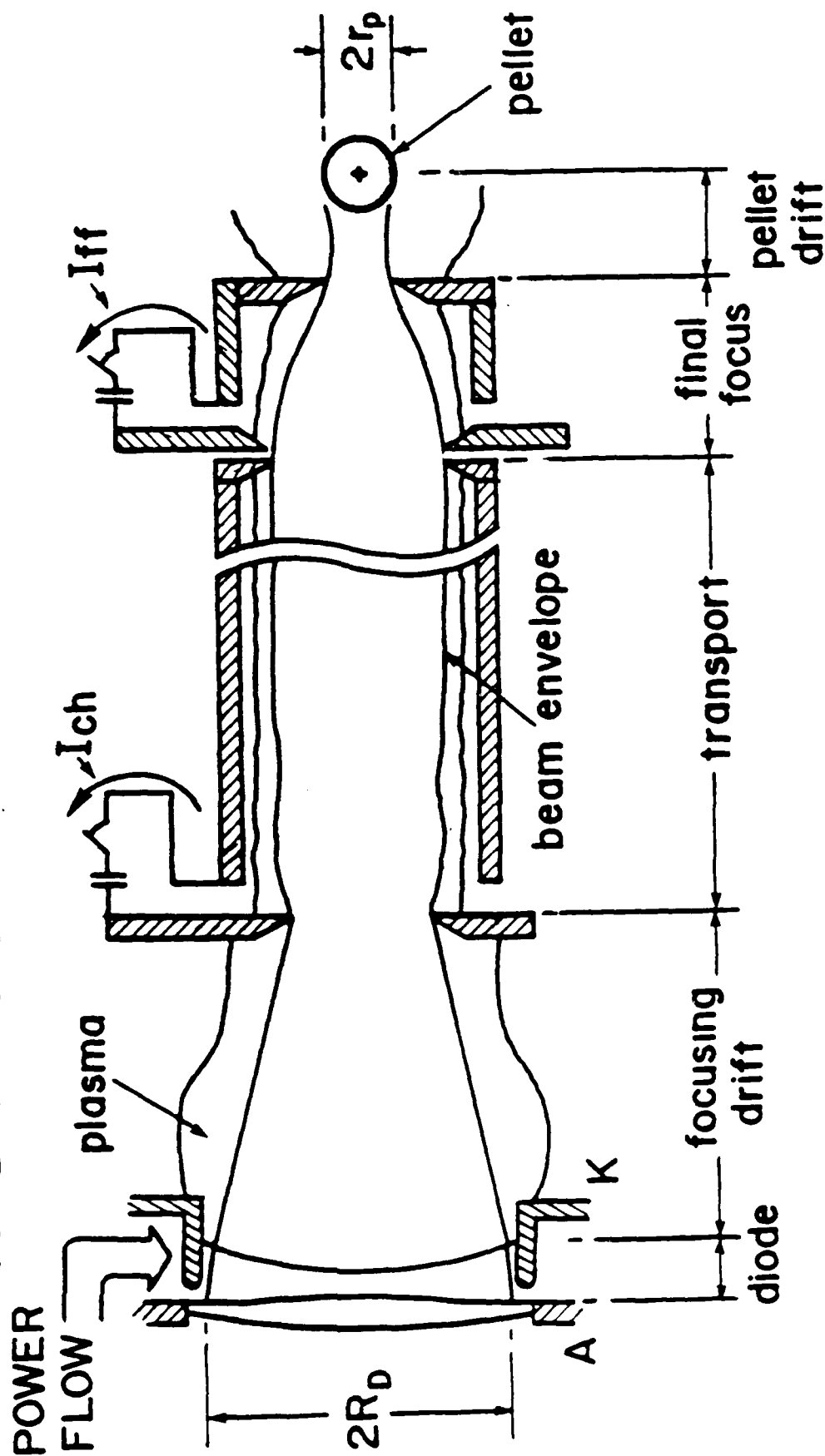


Figure 1 The basic components of the ion beam production, transport, and focusing system.

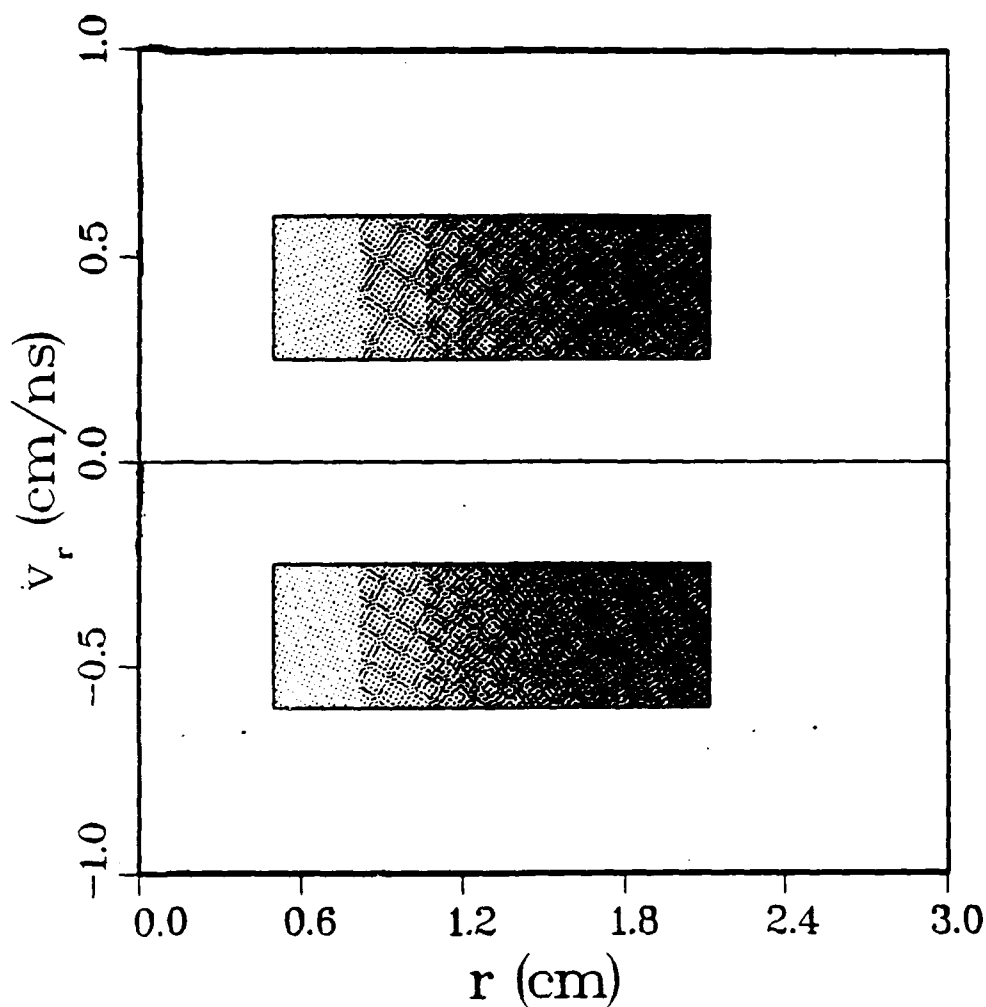


Figure 2 The initial ion beam radial phase space distribution used in the Vlasov equation analysis. Note that because of the cylindrical geometry, the distribution function must be more heavily weighted at large radii to produce a flat number density profile.

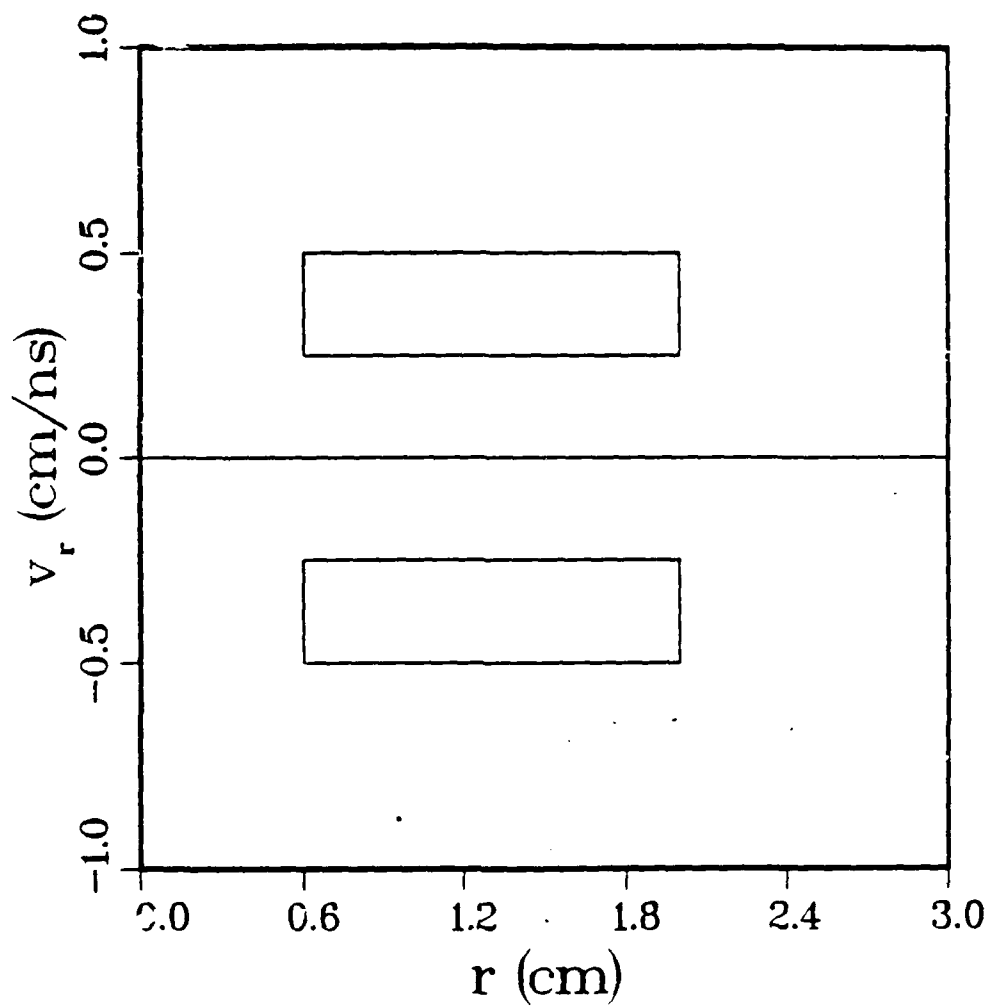


Figure 3a General form of the initial radial phase space distribution corresponding to Eq. (17).

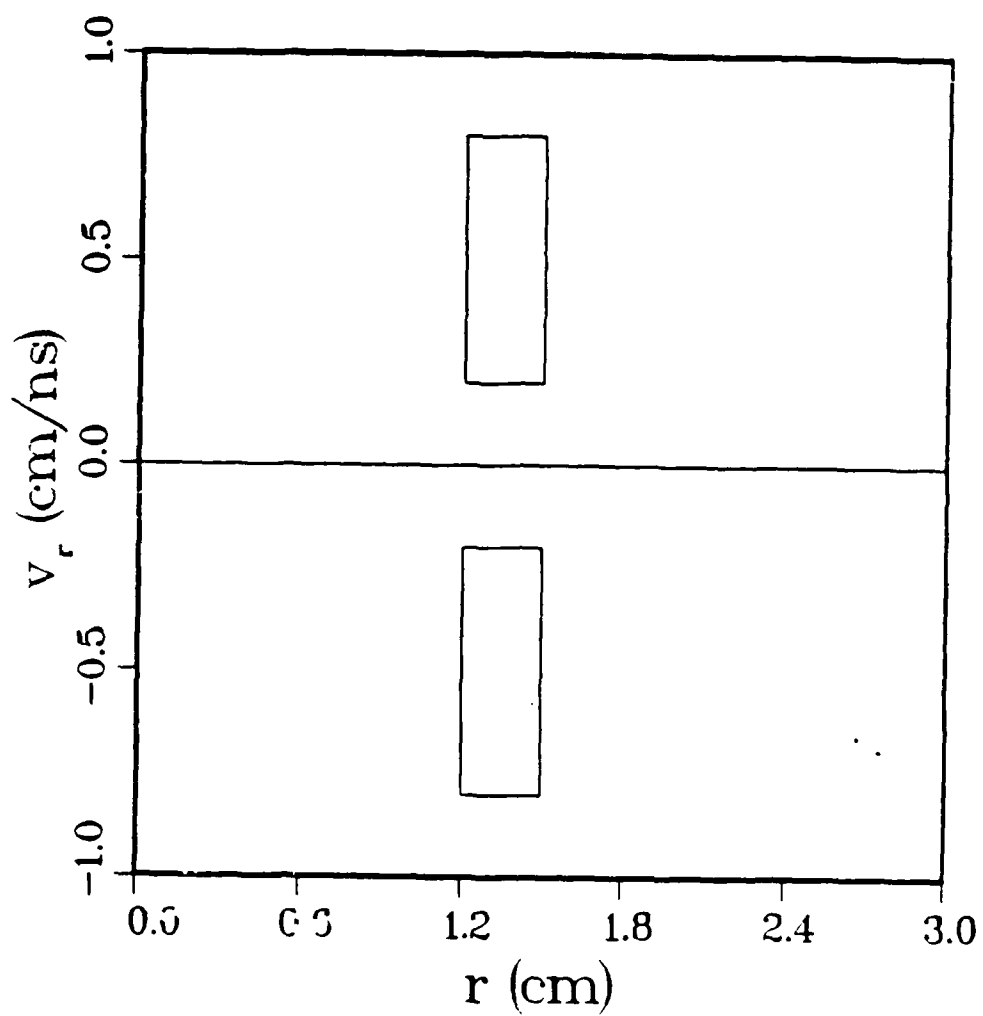


Figure 3b General form of the initial radial phase space distribution corresponding to Eq. (18).

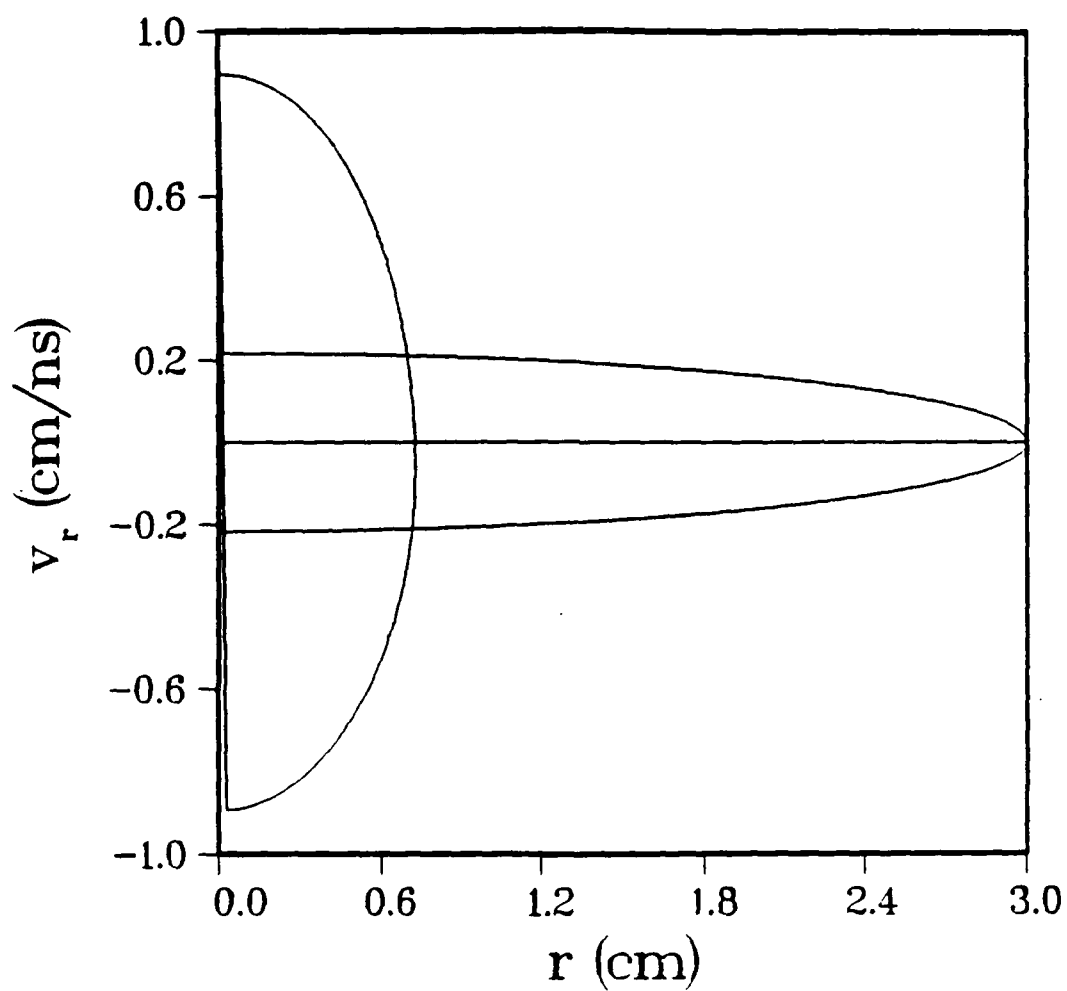


Figure 4a The outer boundary of the radial phase space distribution at the entrance and at the exit of a one-quarter betatron wavelength focusing cell.

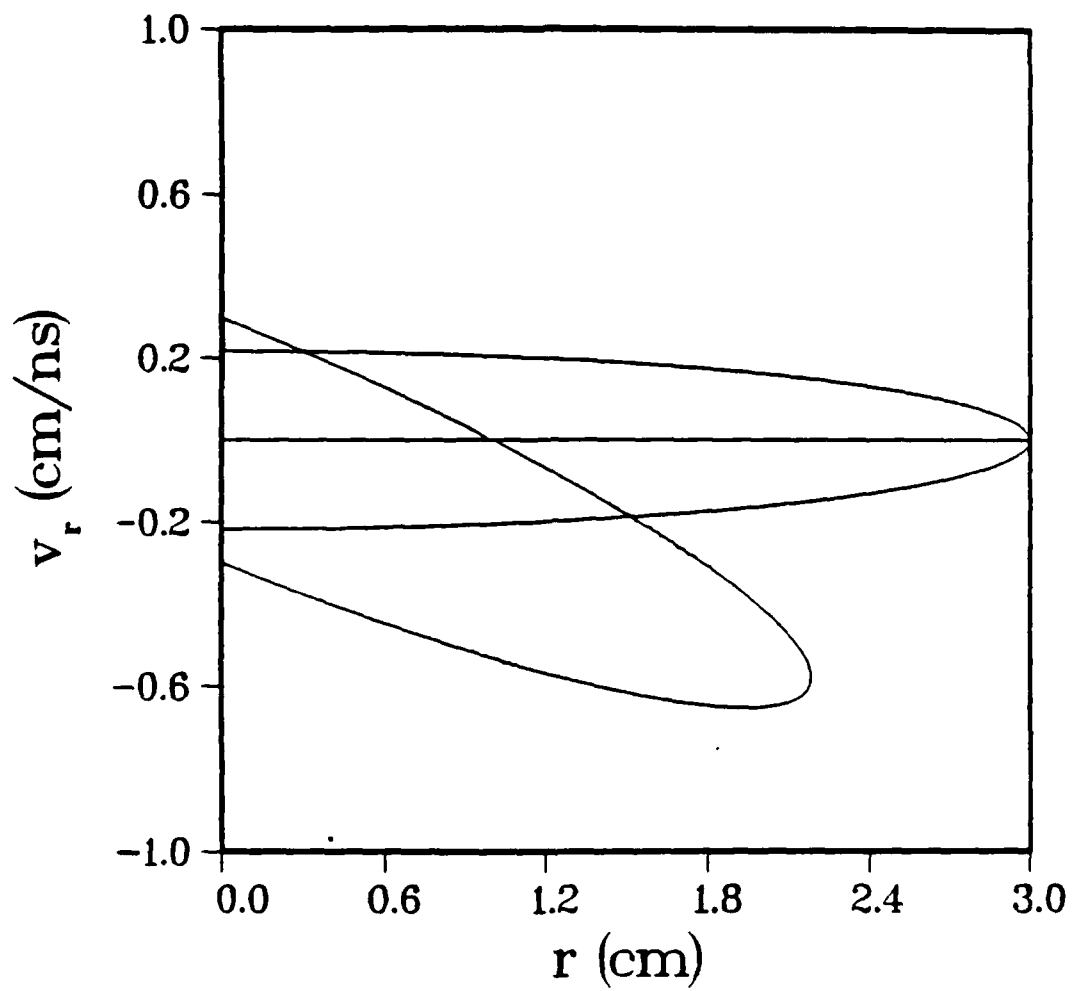


Figure 4b The outer boundary of the radial phase space distribution at the entrance and at the exit of a one-eighth betatron wavelength focusing cell.

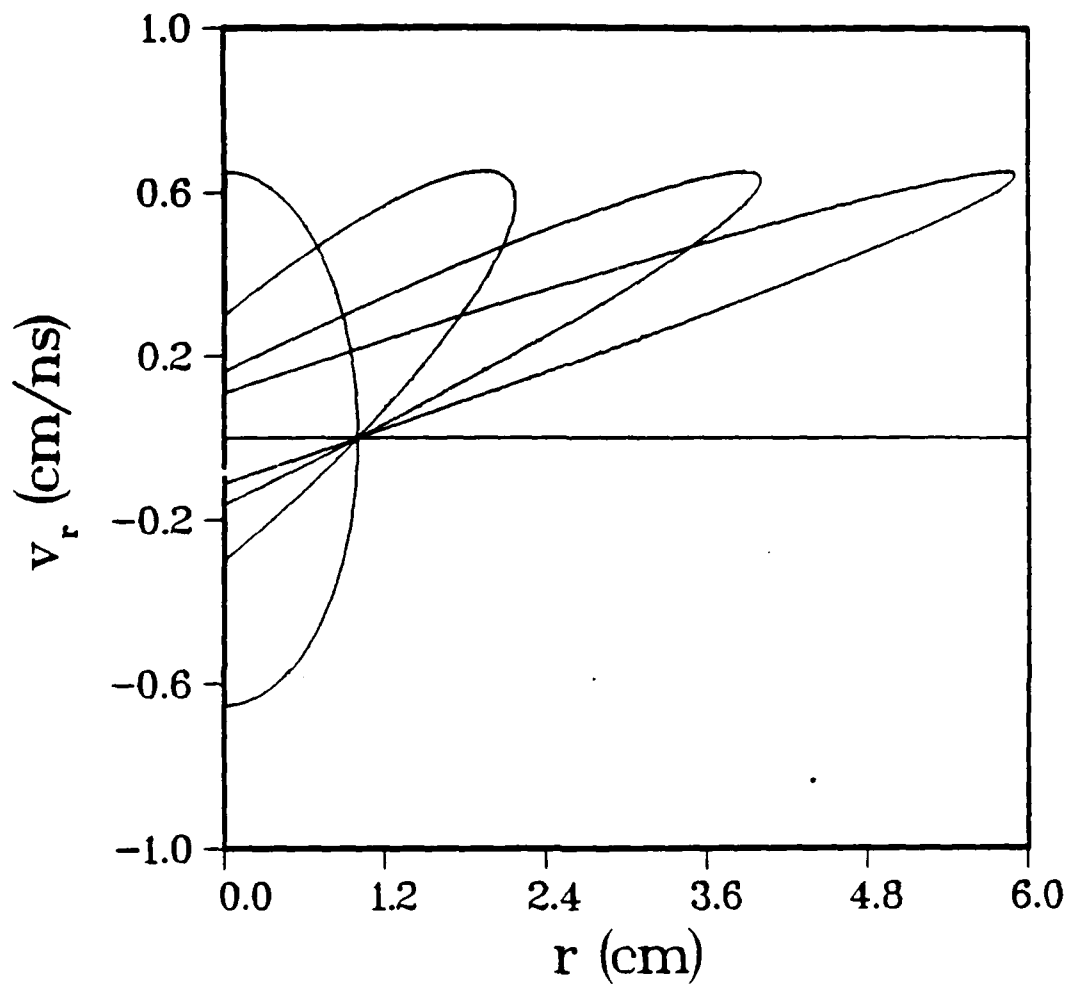


Figure 5 The outer boundary of the radial phase space boundary at several locations in the ballistic drift region. Note that the area inside the boundary curve is constant.

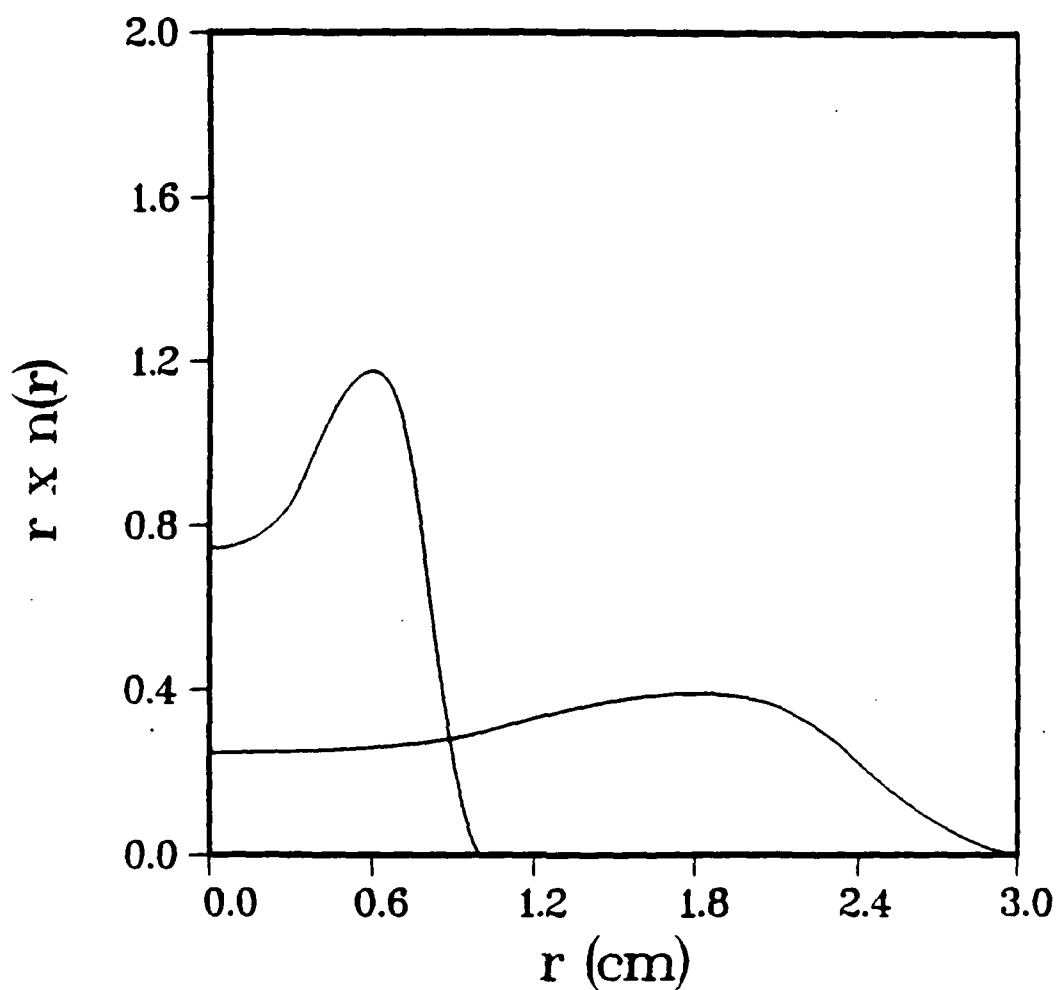


Figure 6a Comparison of $rn(r)$ in the transport channel to $rn(r)$ at the focal plane. In this example, $r_{\max} = 2.121$ cm, $\alpha_{\max} = 0.0535$ rad, $r_{\min} = 0$, and $\alpha_{\min} = 0$; $I_c = 20$ kA, $I_f = 340$ kA, and $r_c = 3$ cm. The ion beam consisted of 30 MeV Li^{+3}_7 .

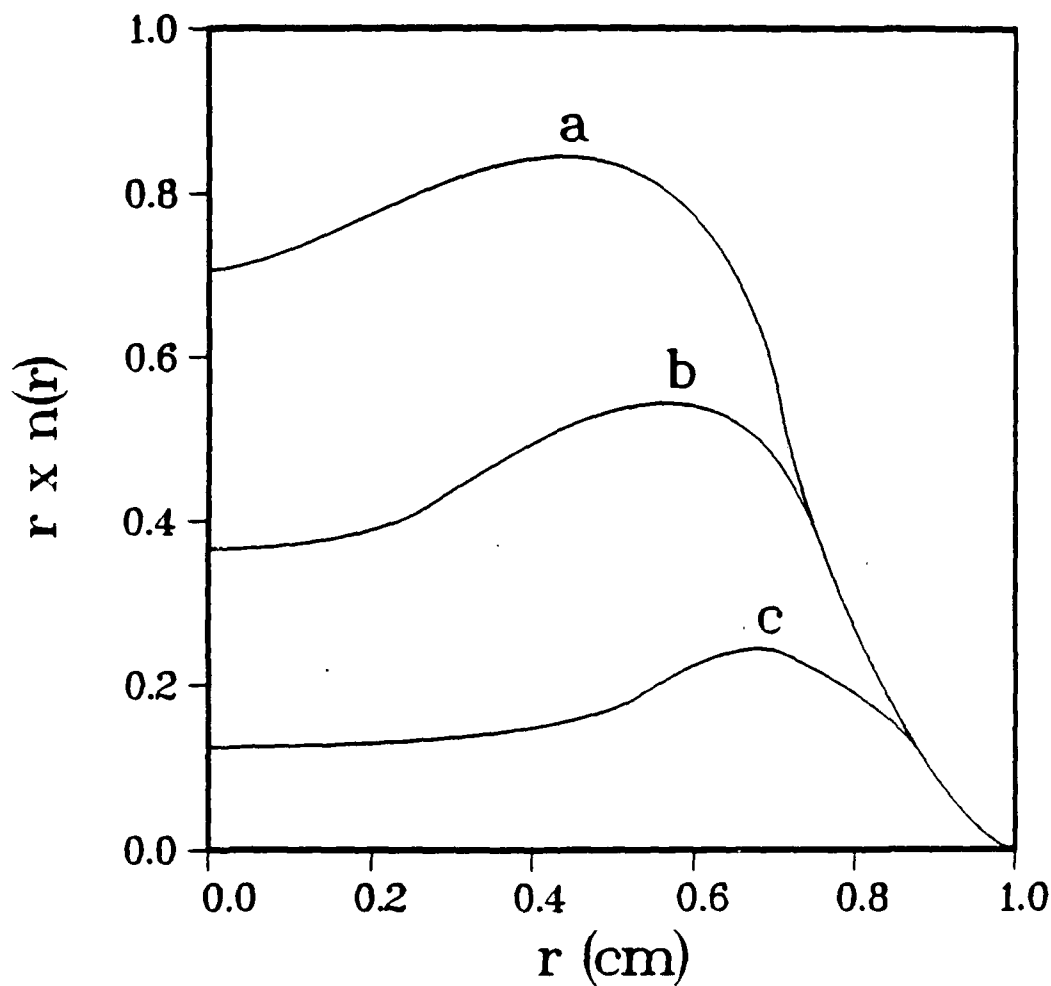


Figure 6b Number density profiles obtained from the distribution given by Eq. (17) with $r_{\max} = 2.121$ cm, $\alpha_{\max} = 0.0535$ radians, $r_{\min} = 0.0$ cm, and (a) $\alpha_{\min} = 0.0$ radians, (b) $\alpha_{\min} = 0.02$ radians, and (c) $\alpha_{\min} = 0.04$ radians.

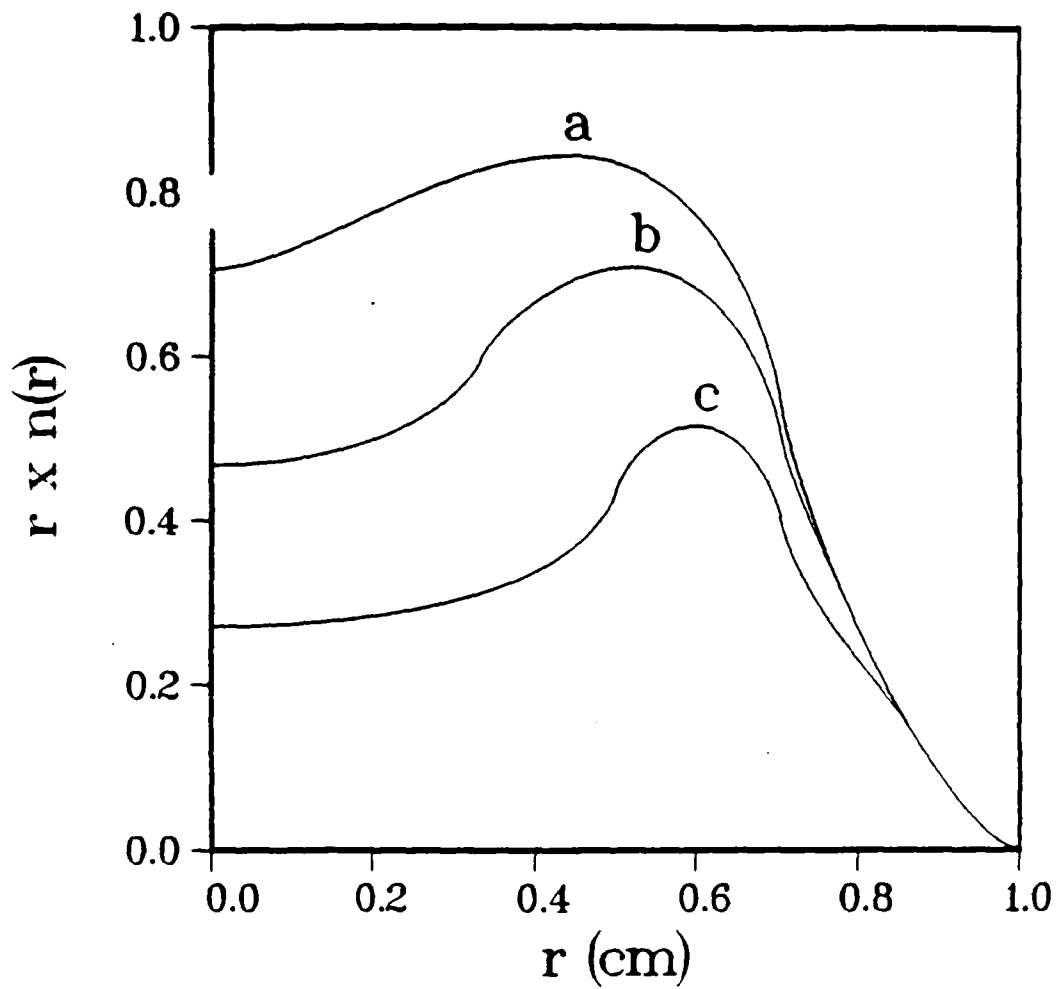


Figure 7 Number density profiles obtained from the distribution given by Eq. (17) with $r_{\max} = 2.121$ cm, $\alpha_{\max} = 0.0535$ radians, $\alpha_{\min} = 0.0$ radians for (a) $r_{\min} = 0$, (b) $r_{\min} = 1.0$ cm, and (c) $r_{\min} = 1.5$ cm.

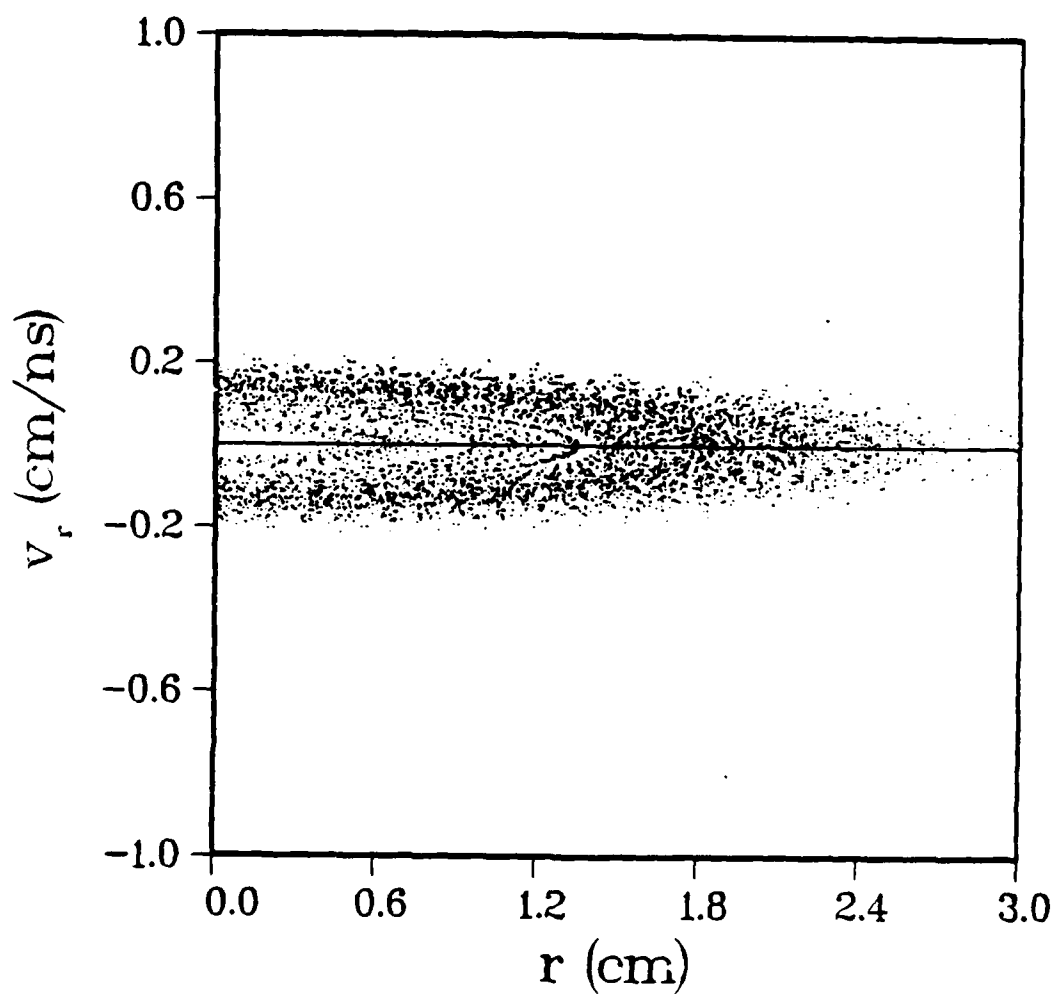


Figure 8a Radial phase space distribution for the zero angular momentum beam in the phase mixed state at the entrance to the final focusing cell. 5100 particles were used.

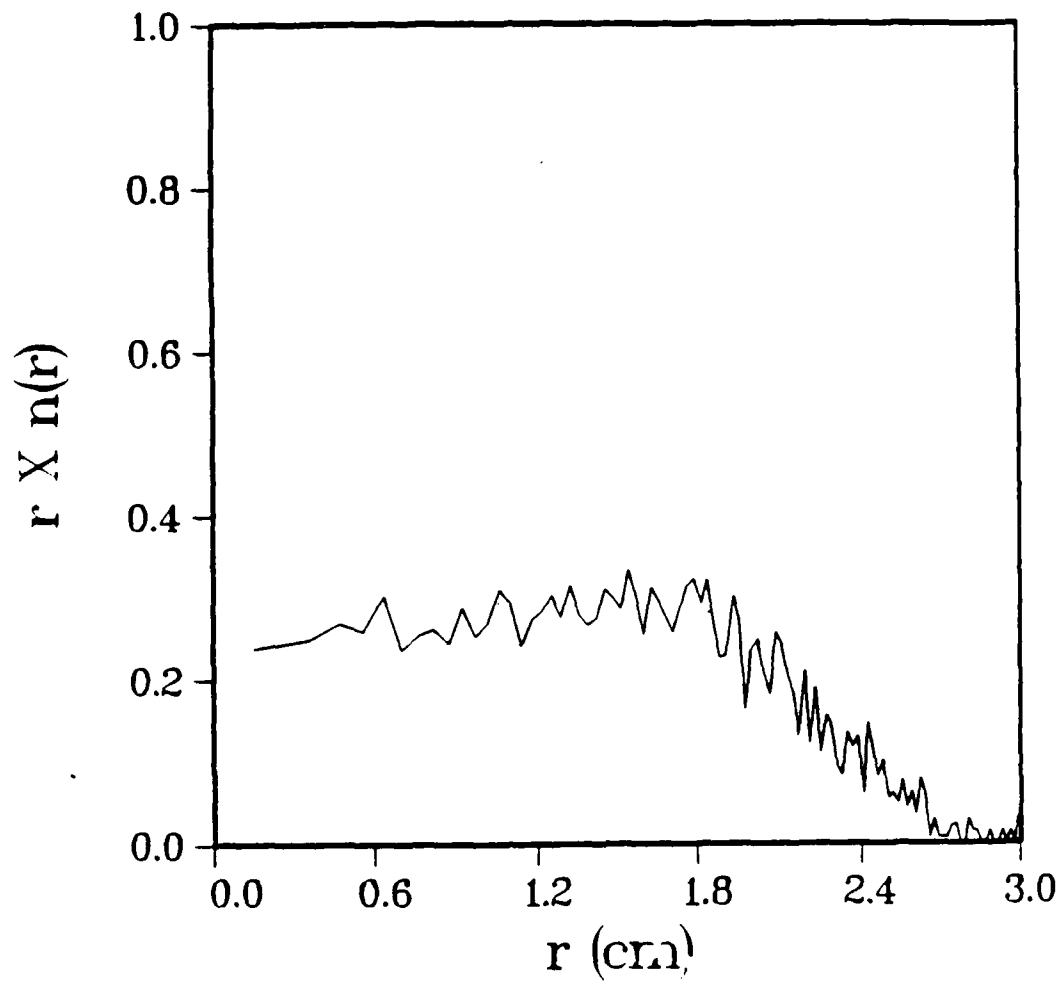


Figure 8b $rn(r)$ profile for the zero angular momentum beam in the phase mixed state at the entrance to the final focusing cell.

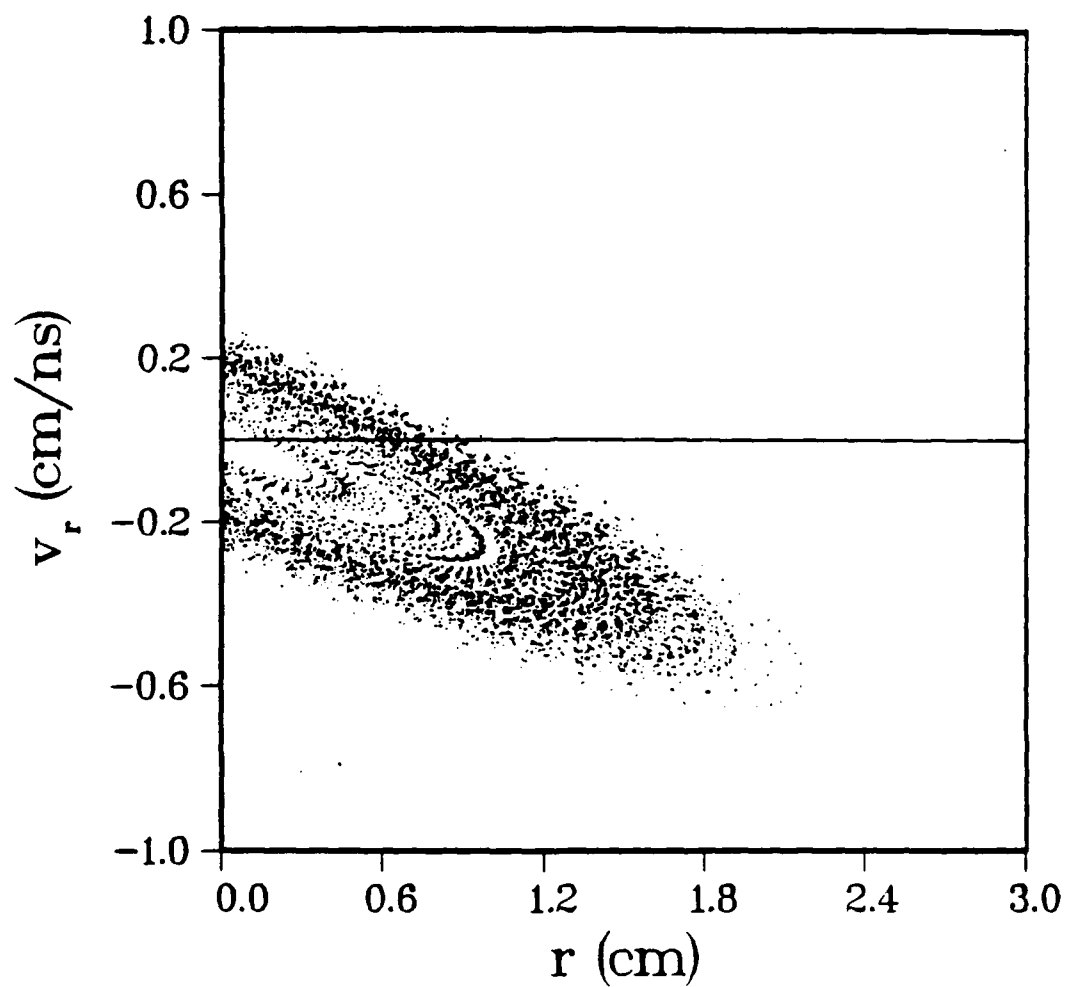


Figure 9a Radial phase space distribution for the zero angular momentum beam at the final focusing cell exit.

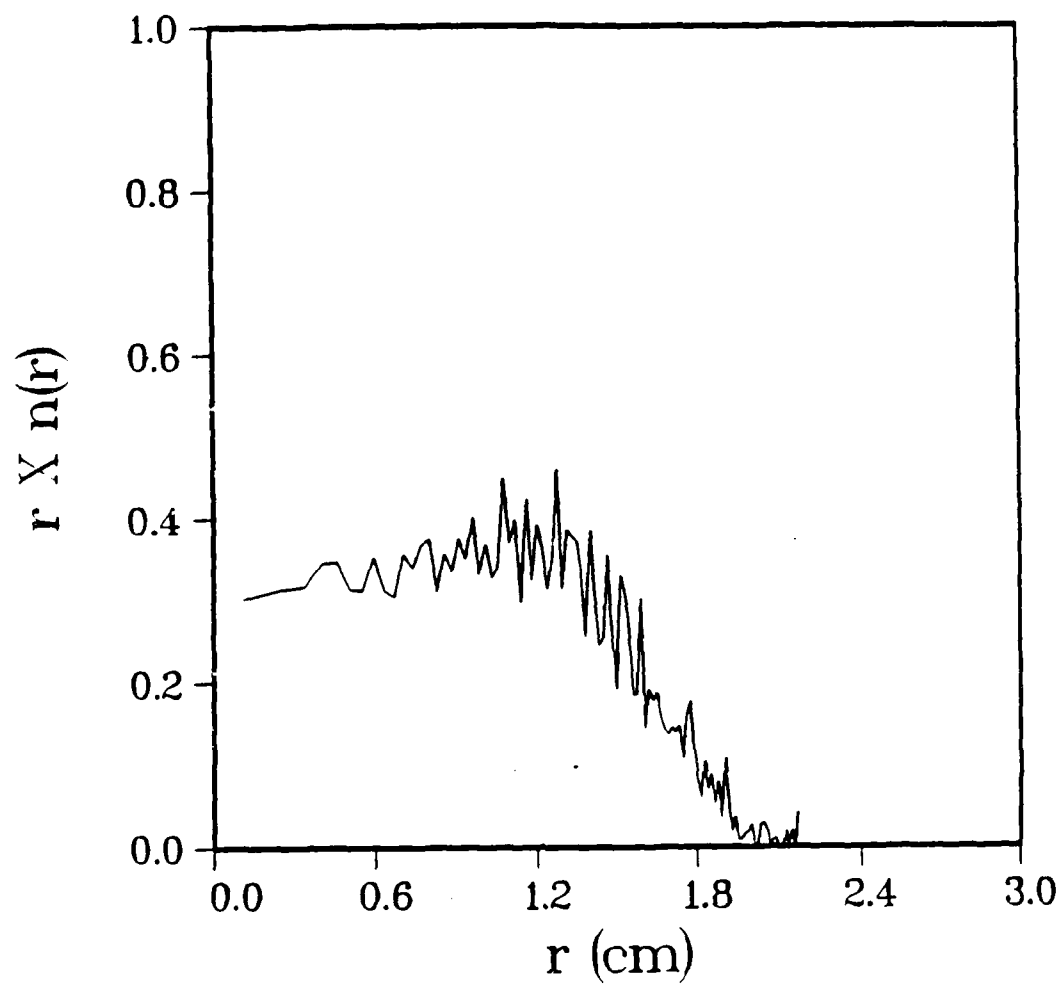


Figure 9b $rn(r)$ profile for the zero angular momentum beam at the final focusing cell exit.

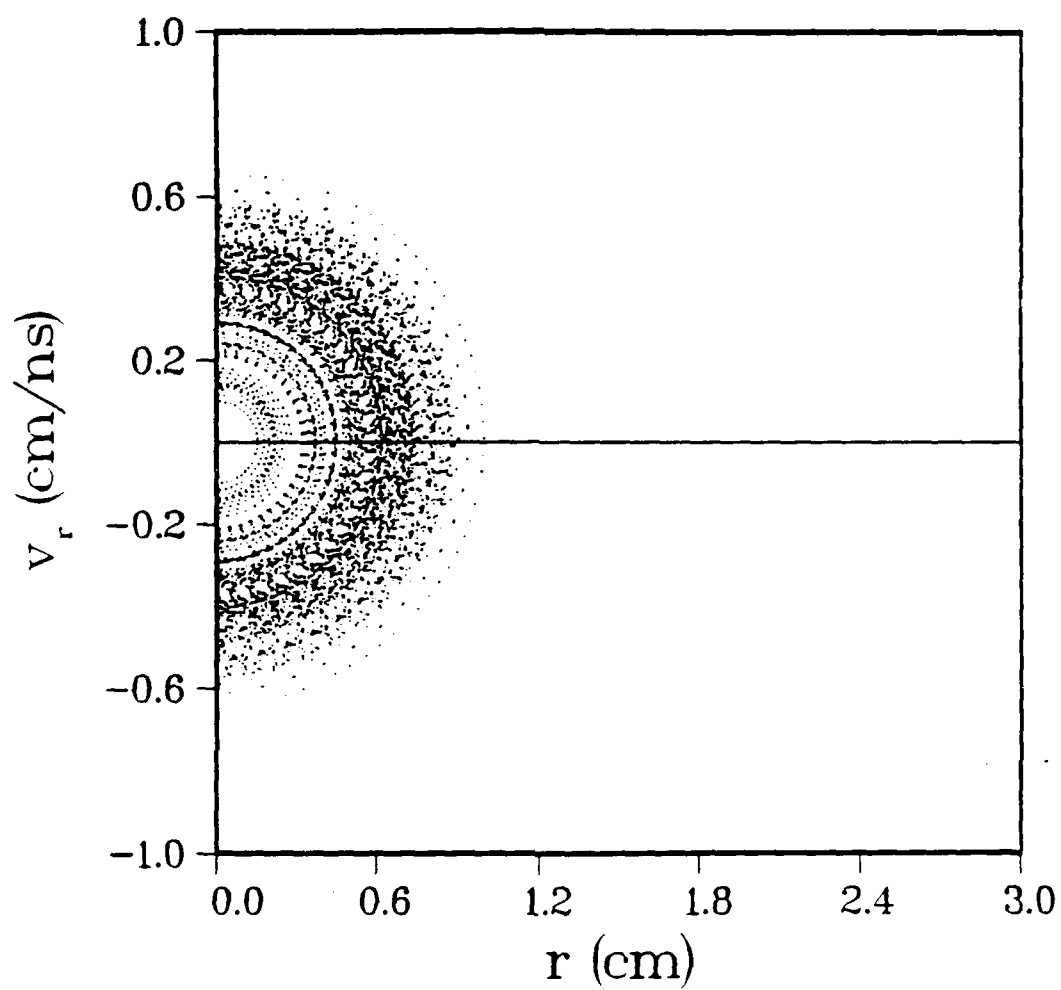


Figure 10a Radial phase space distribution for the zero angular momentum beam at the focal plane.

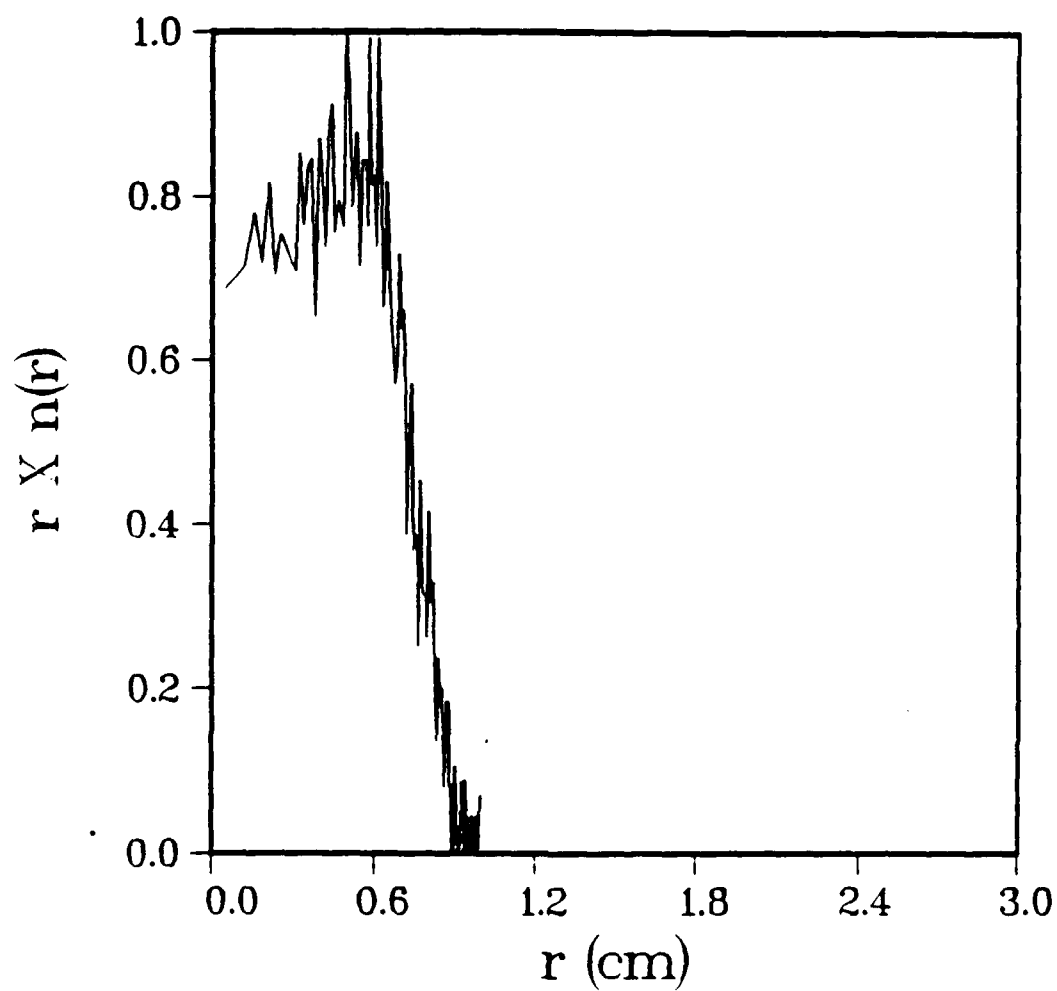


Figure 10b $rn(r)$ profile for the zero angular momentum beam at the focal plane.

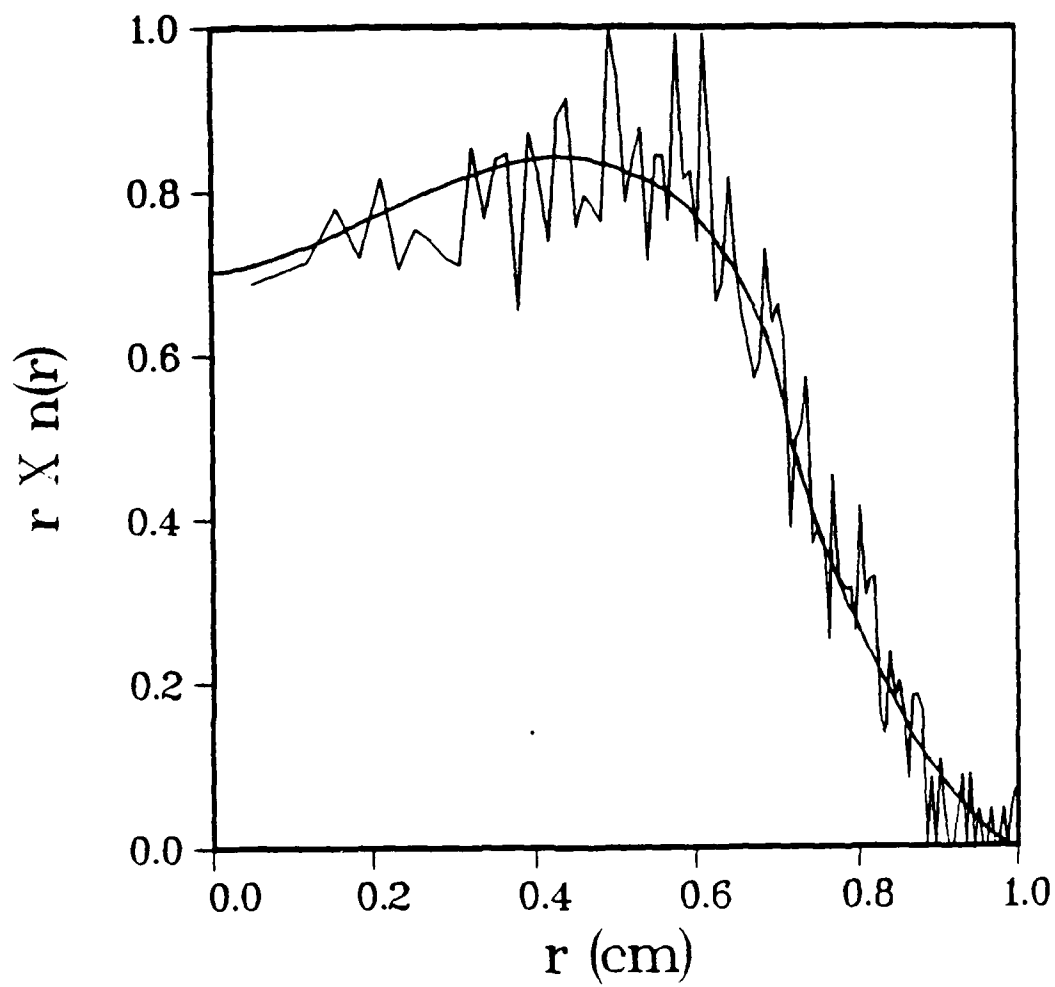


Figure 10c $rn(r)$ profile for the zero angular momentum beam at the focal plane shown on an expanded scale along with the theoretically predicted result.

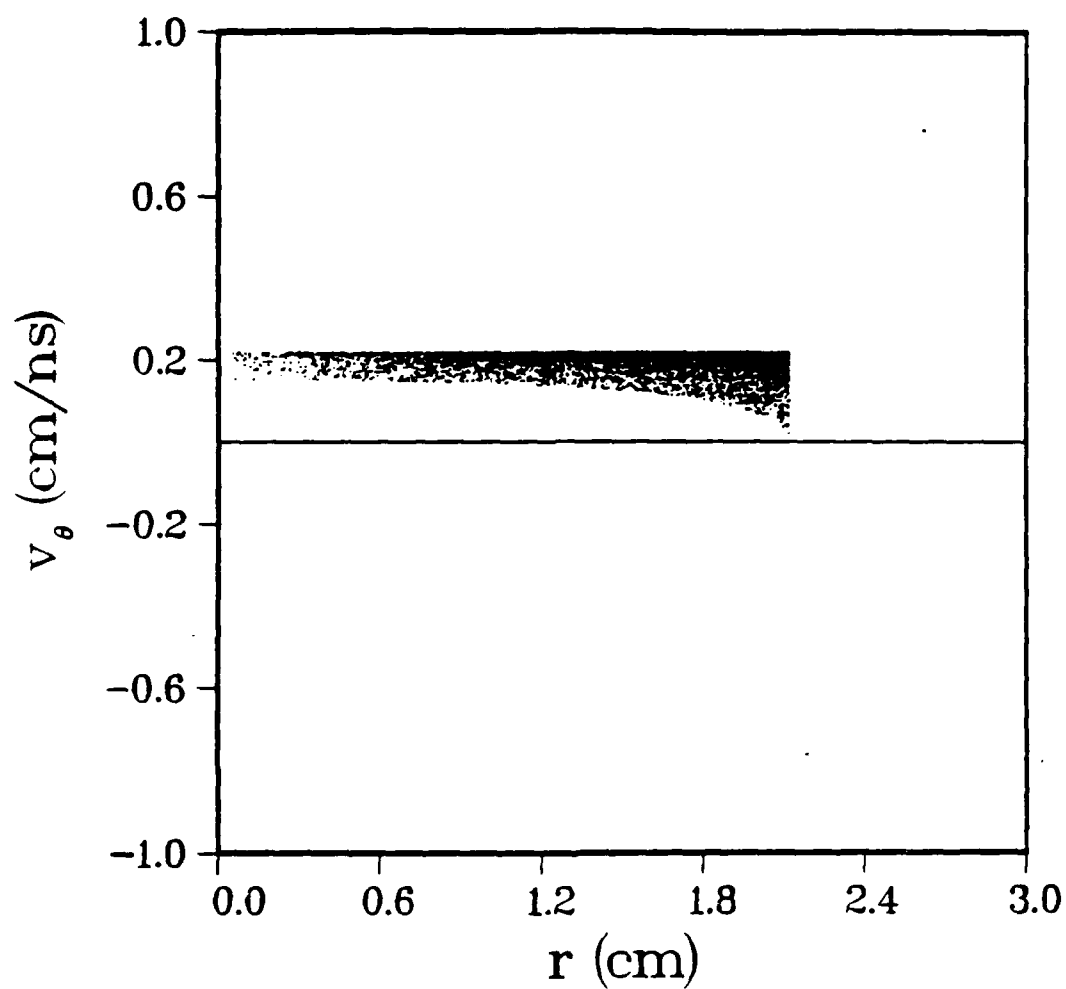


Figure 11 Distribution of particles in the r - v_θ plane at the entrance to the transport channel for the maximum angular momentum simulation.

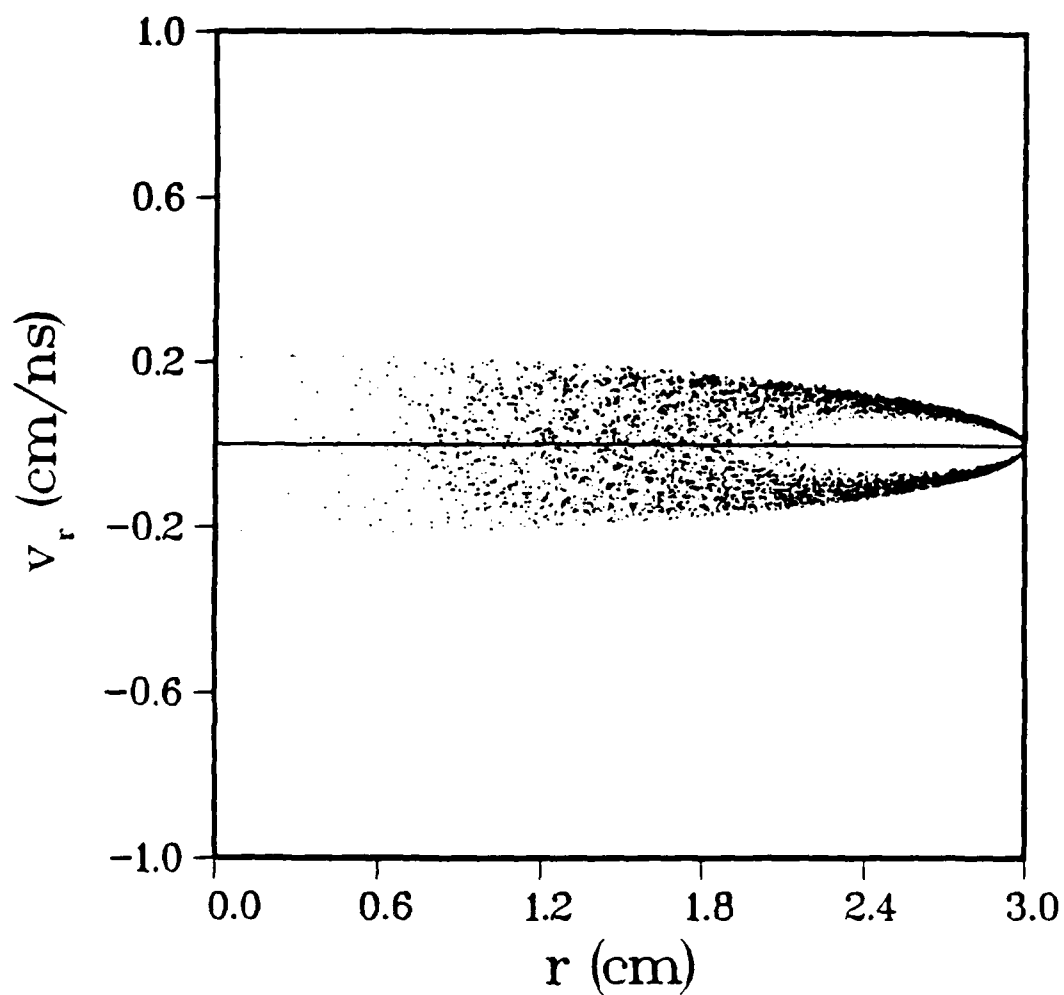


Figure 12a Radial phase space distribution for the maximum angular momentum beam in the phase mixed state at the entrance to the final focusing cell. 5100 ions were used in this simulation.

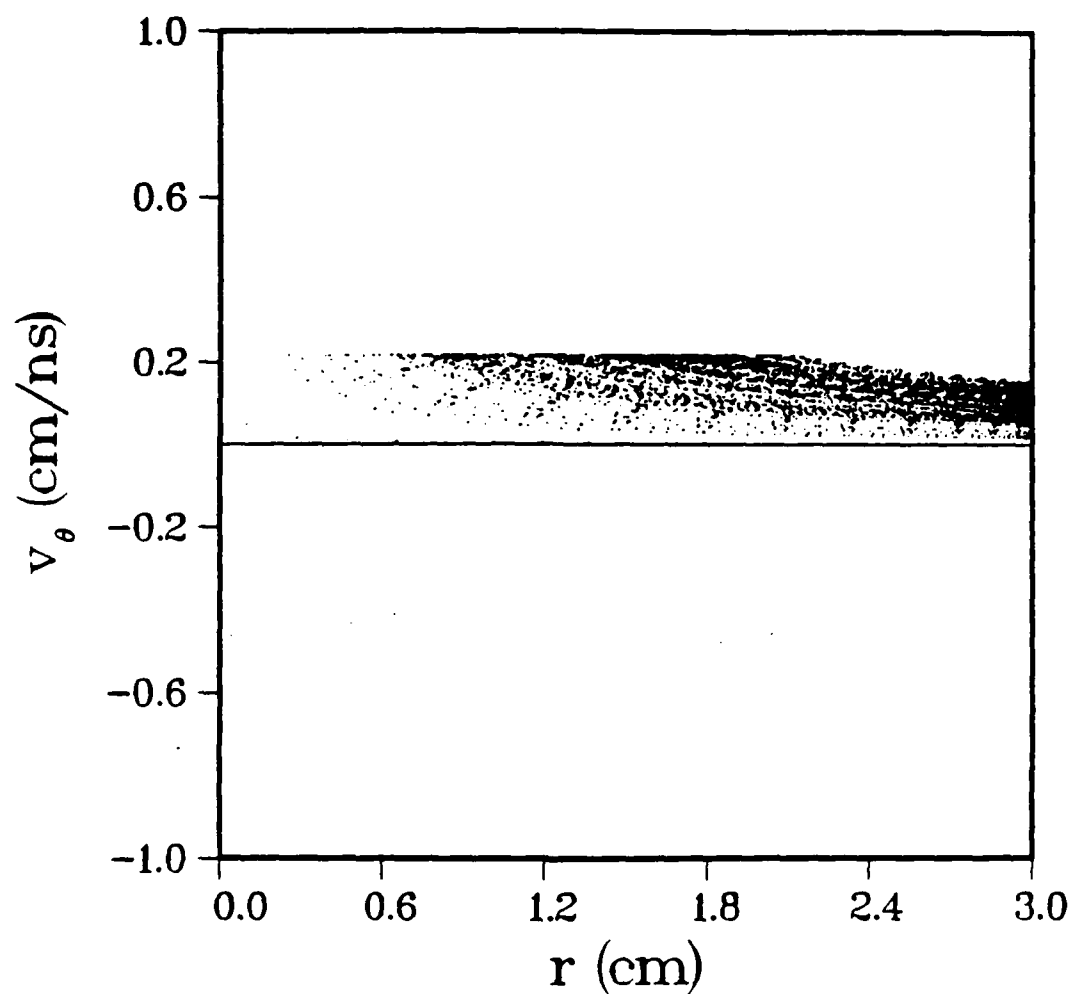


Figure 12b Distribution of particles in the r - v_θ plane for the maximum angular momentum in the phase mixed state at the entrance to the final focusing cell.

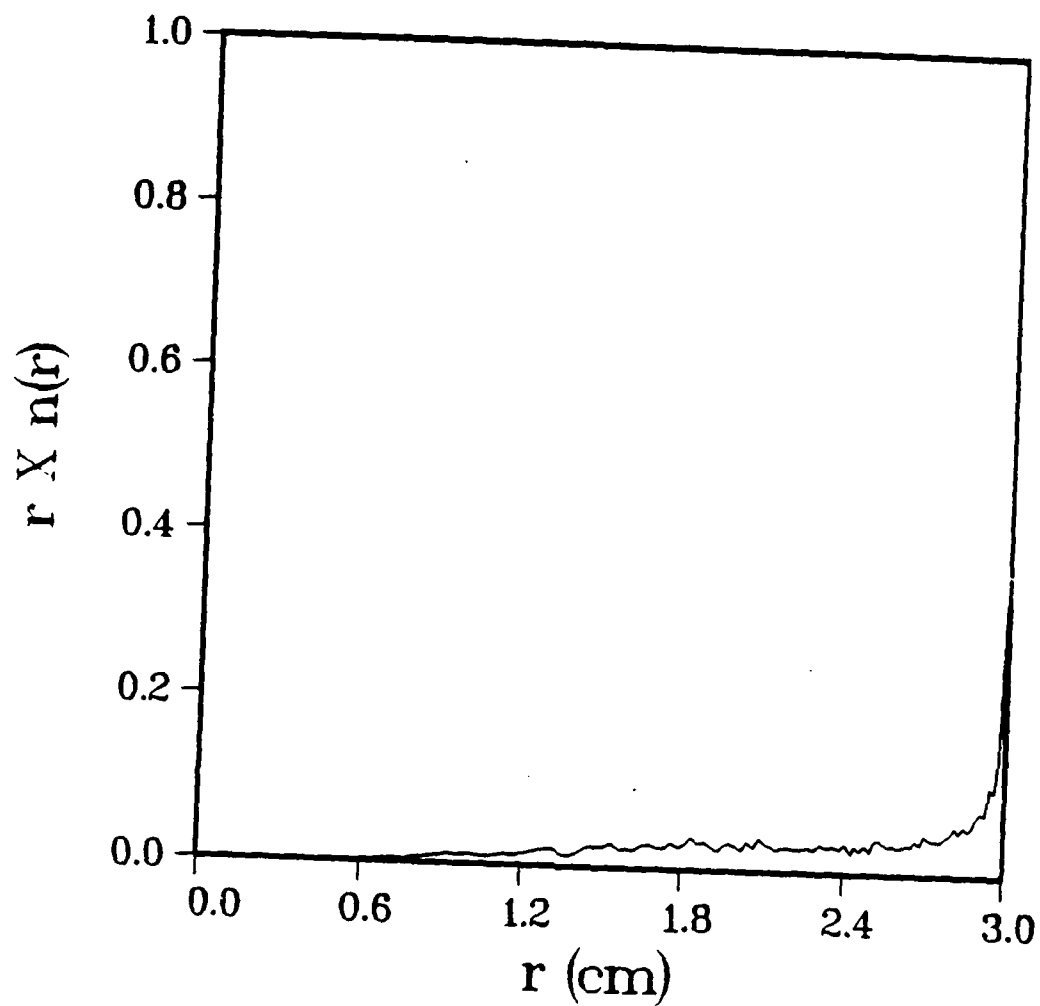


Figure 12c $rn(r)$ profile for the maximum angular momentum beam in the phase mixed state at the entrance to the final focusing.

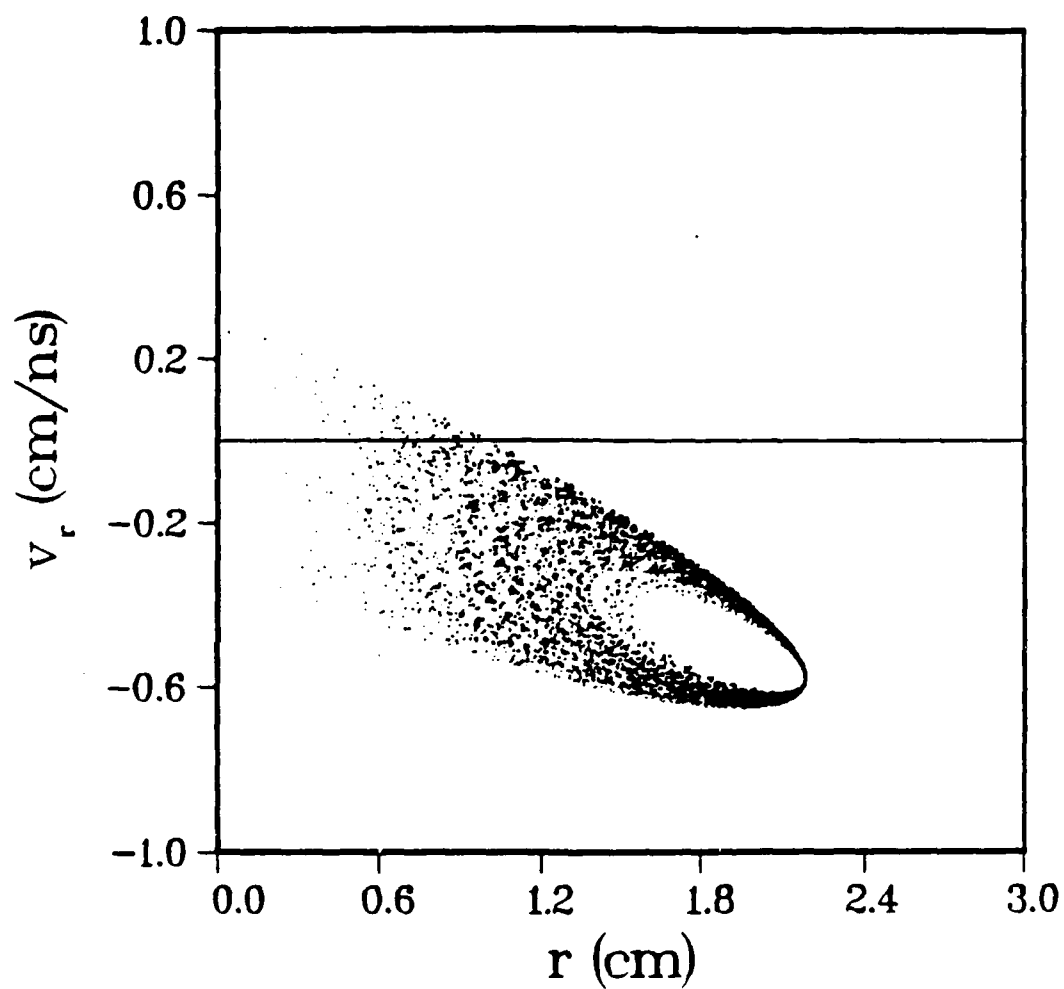


Figure 13a Radial phase space distribution of the maximum angular momentum ion beam at the final focusing cell exit.

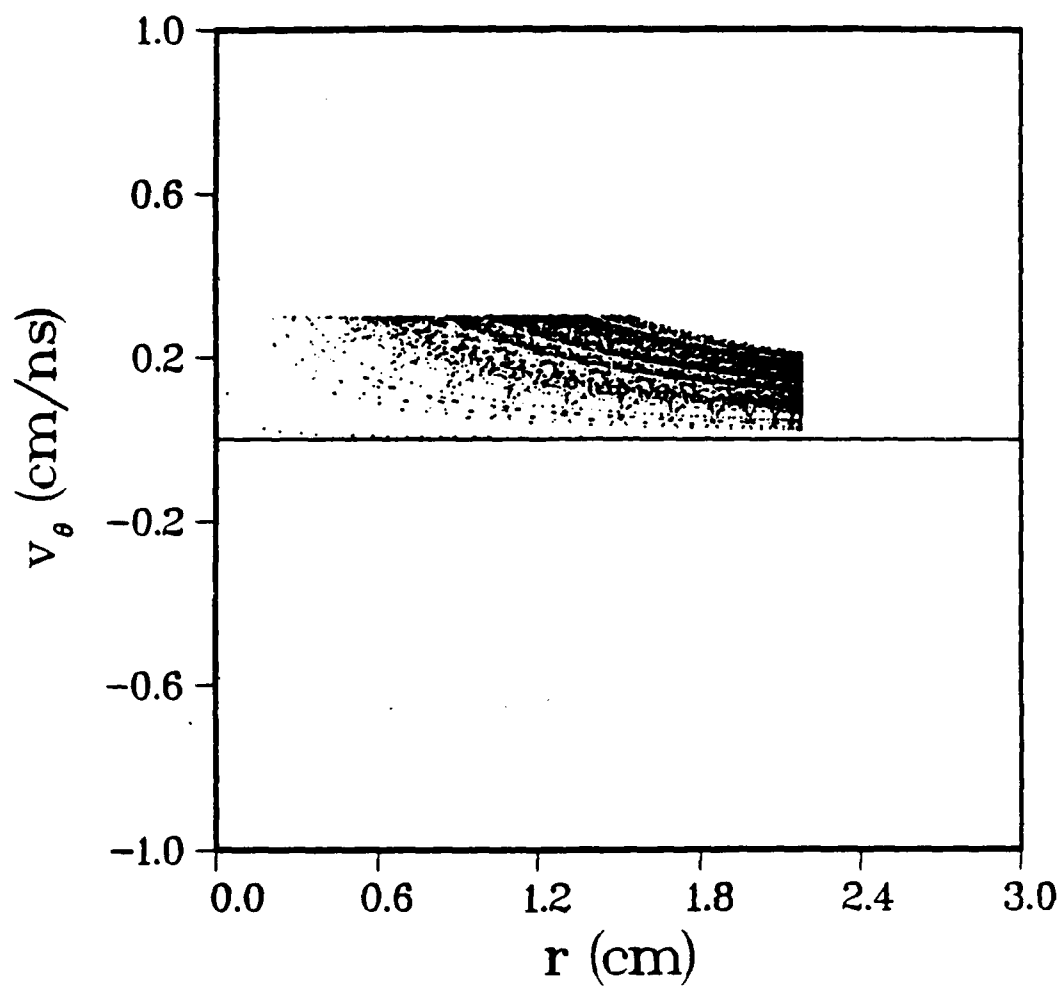


Figure 13b The distribution of ions in the r - v_θ plane for the maximum angular momentum ion beam at the exit of the final focusing cell.

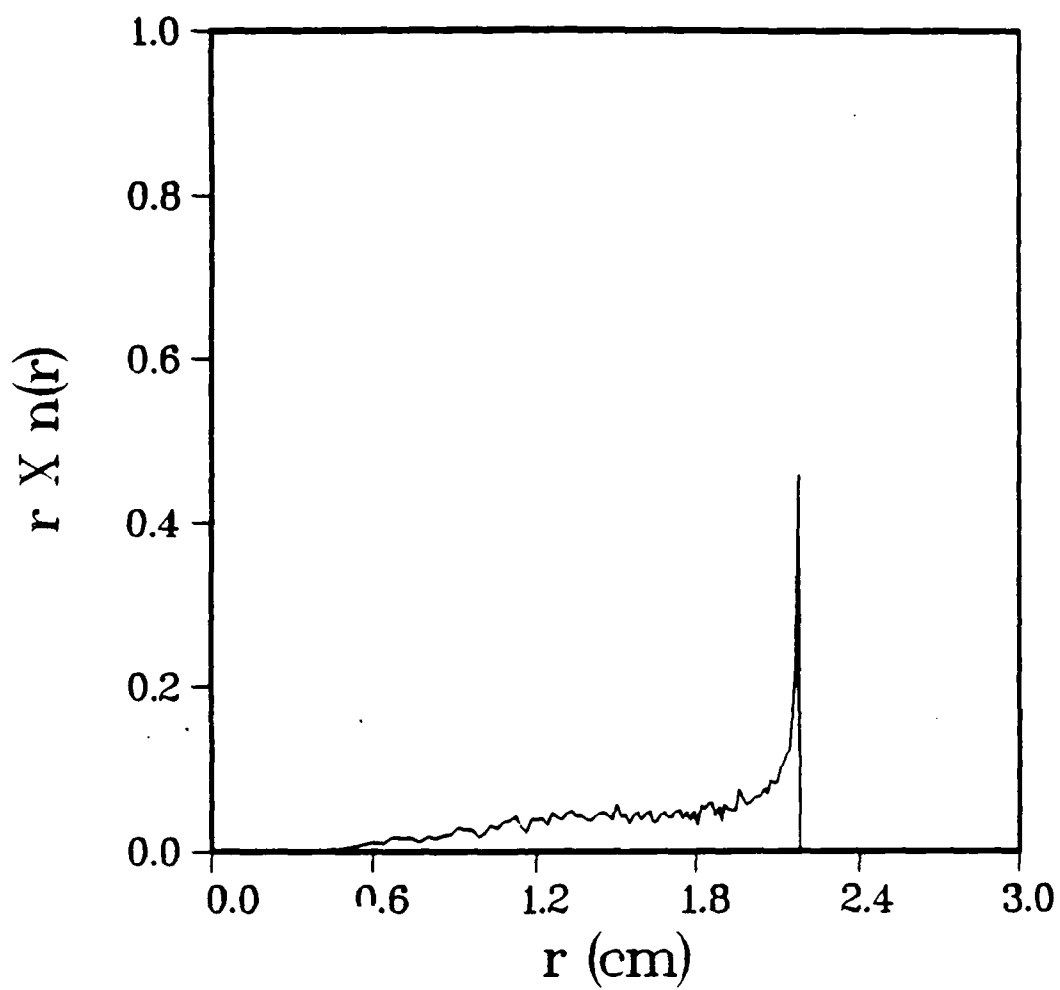


Figure 13c The $r n(r)$ profile for the maximum angular momentum ion beam at the exit of the final focusing cell.

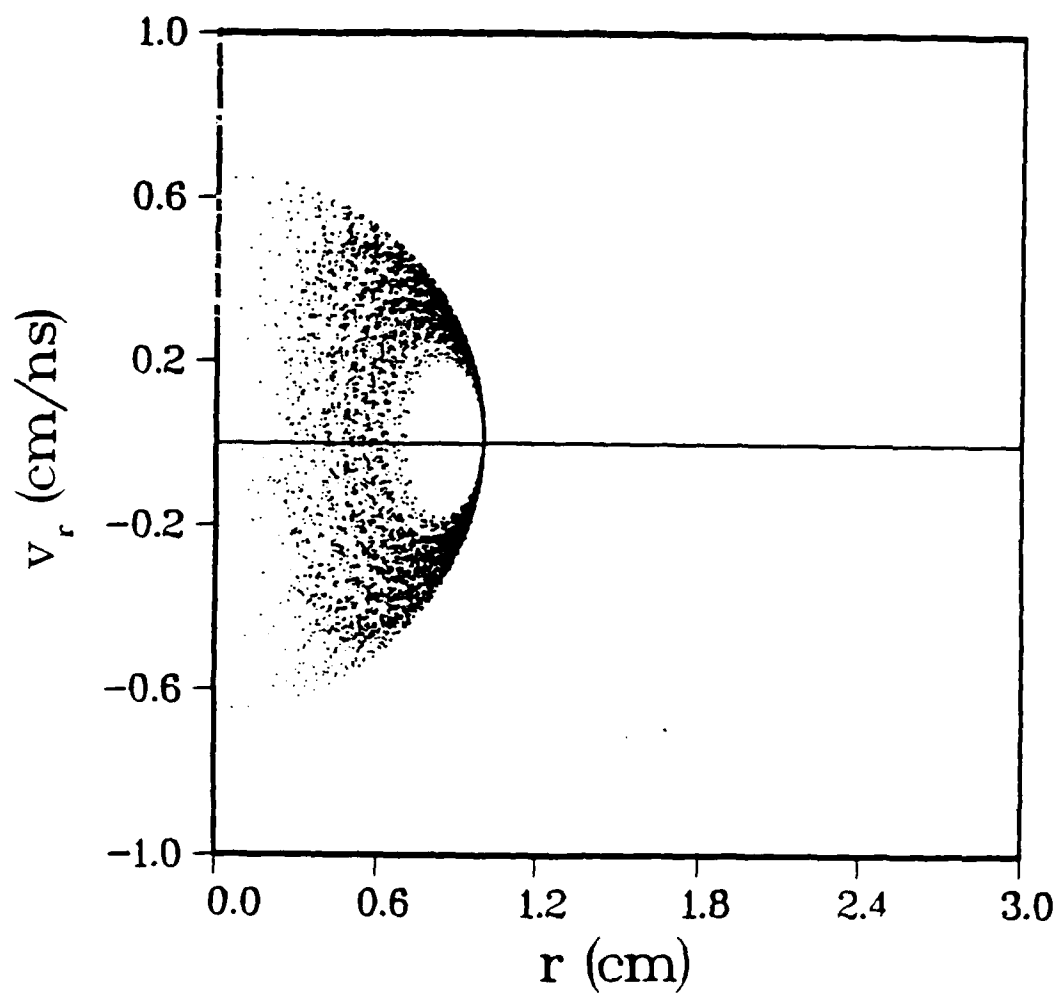


Figure 14a Radial phase space distribution of the maximum angular momentum ion beam at the theoretical focal plane.

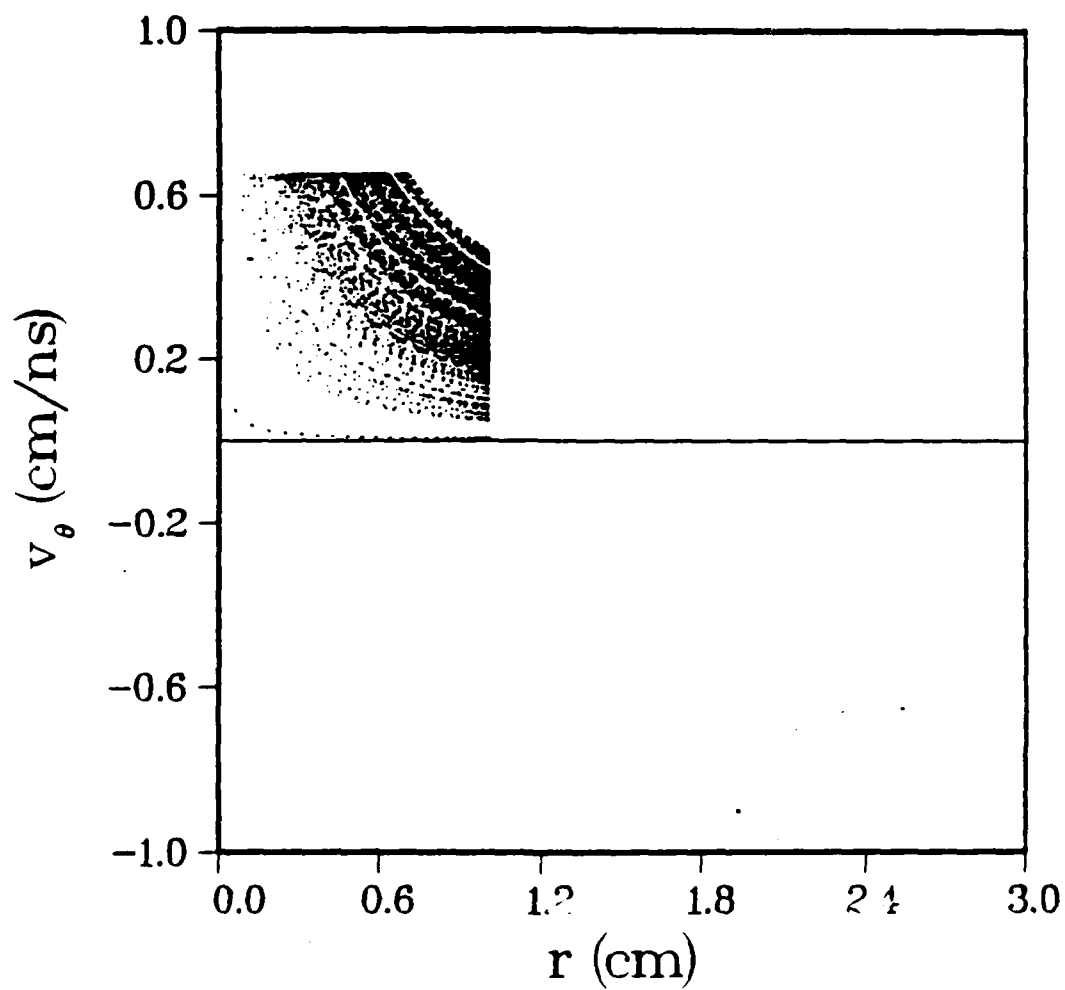


Figure 14b The distribution of ions in the r - v_θ plane for the maximum angular momentum ion beam at the theoretical focal plane.

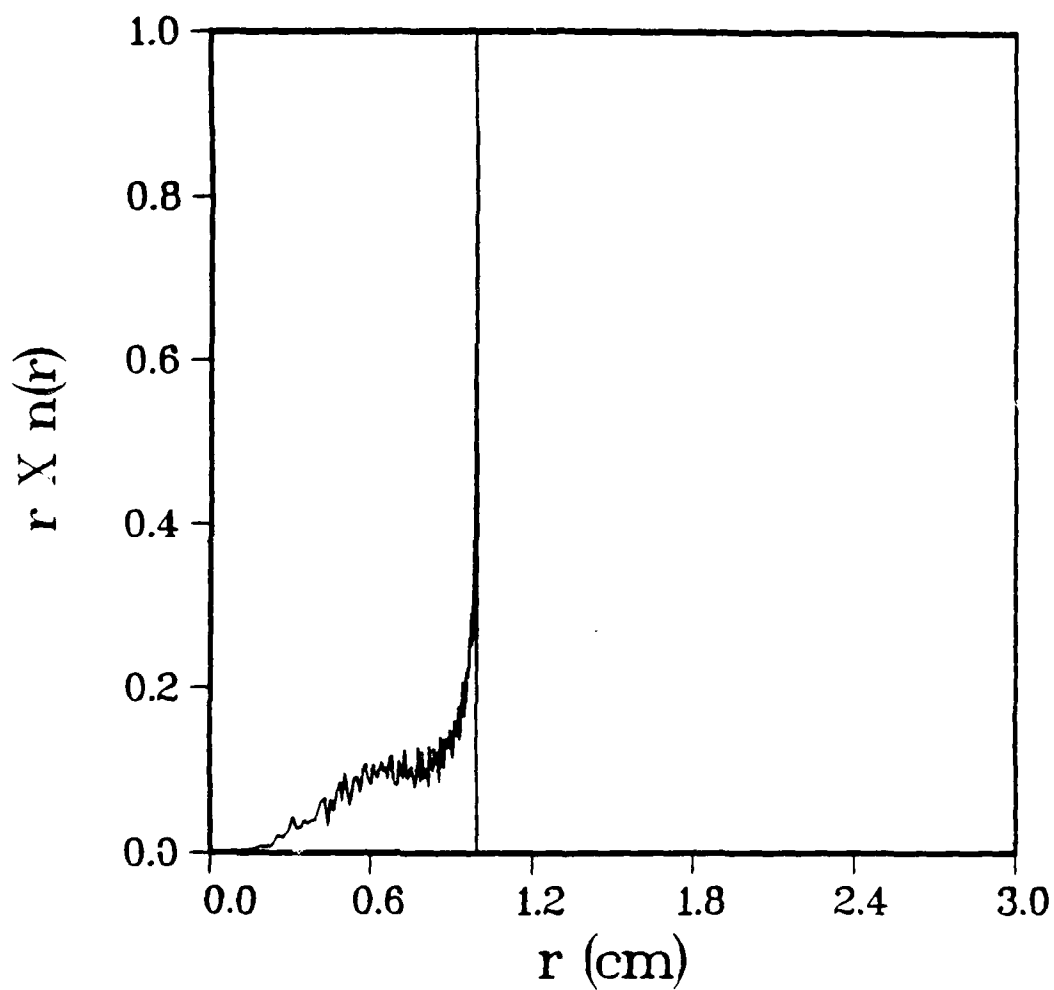


Figure 14c The $rn(r)$ profile for the maximum angular momentum ion beam at the exit of the theoretical focal plane.

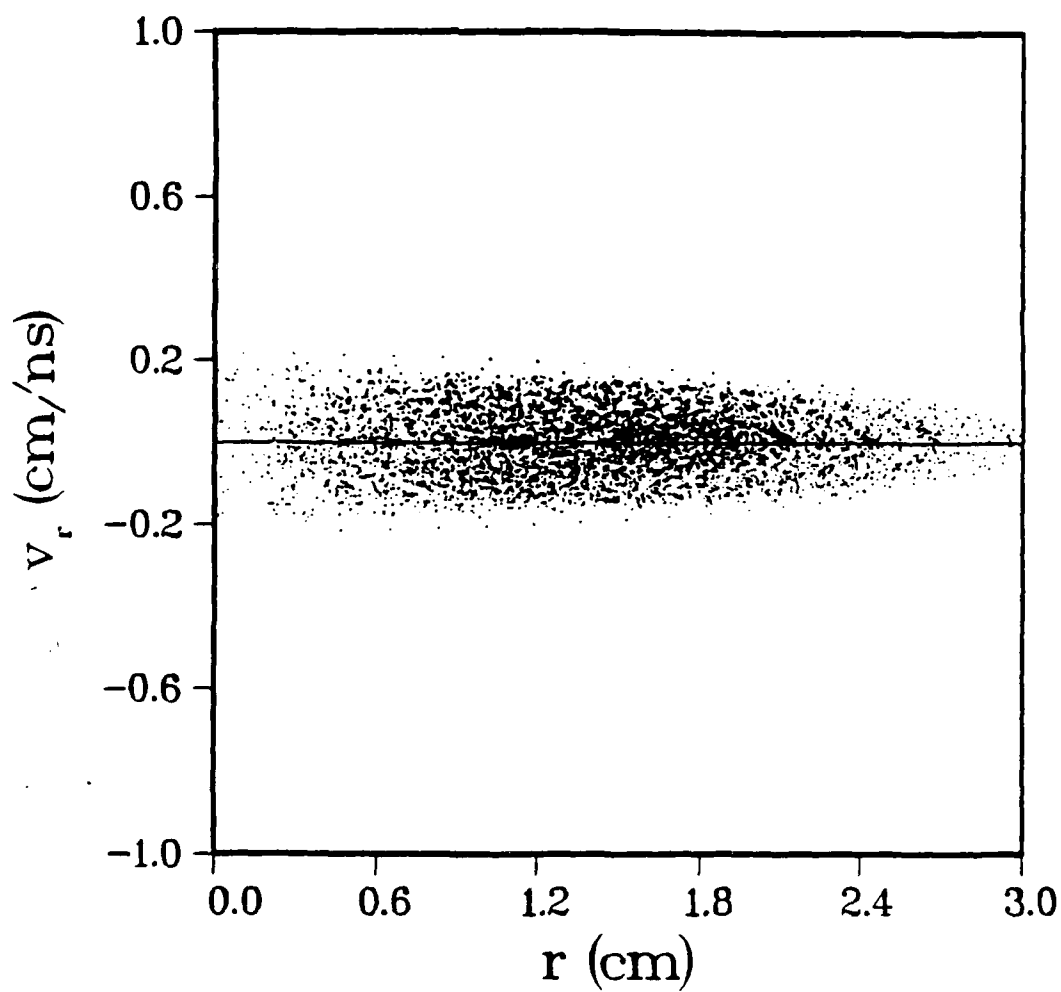


Figure 15a Distribution of ions in the r - v_r plane for the ion beam with initial spread in v_θ comparable to the initial spread in v_r after phase mixing.

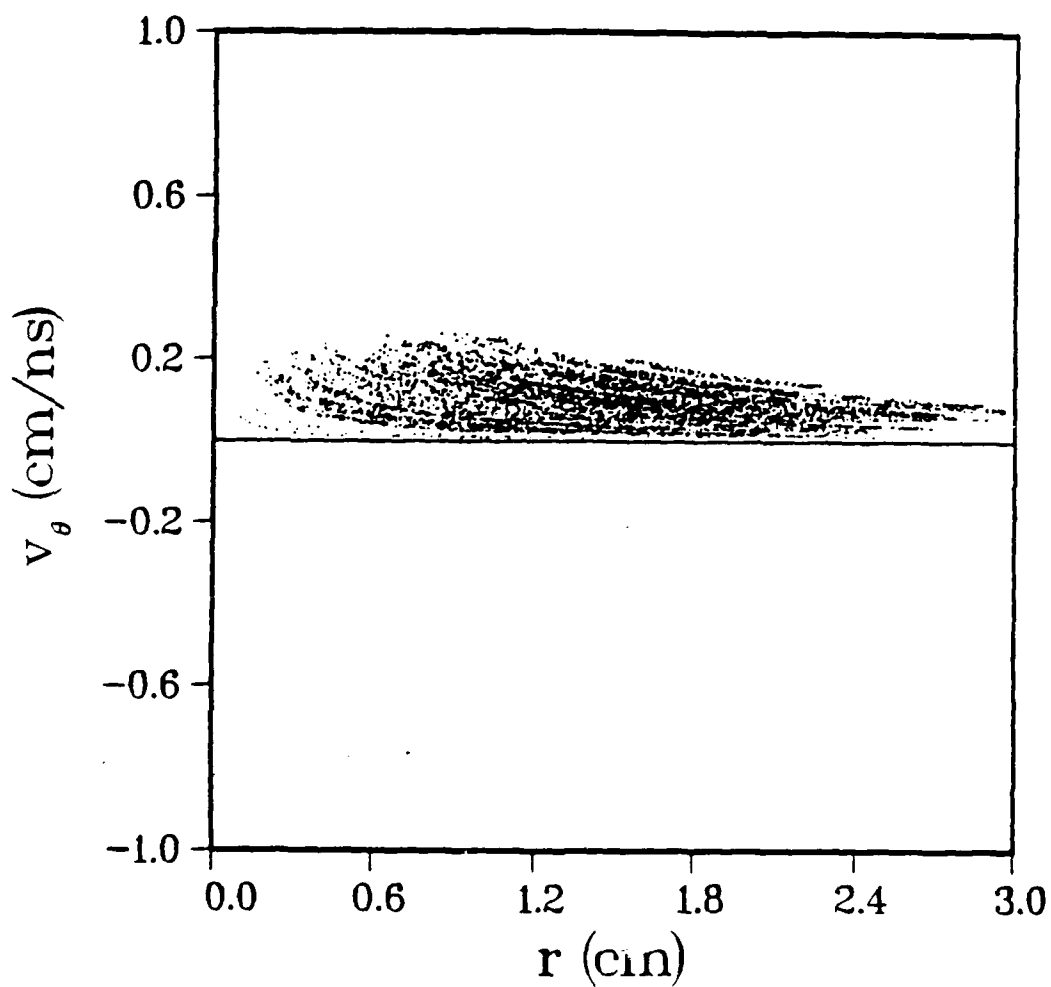


Figure 15b Distribution of ions in the r - v_θ plane for the ion beam with initial spread in v_θ comparable to the initial spread in v_r after phase mixing.

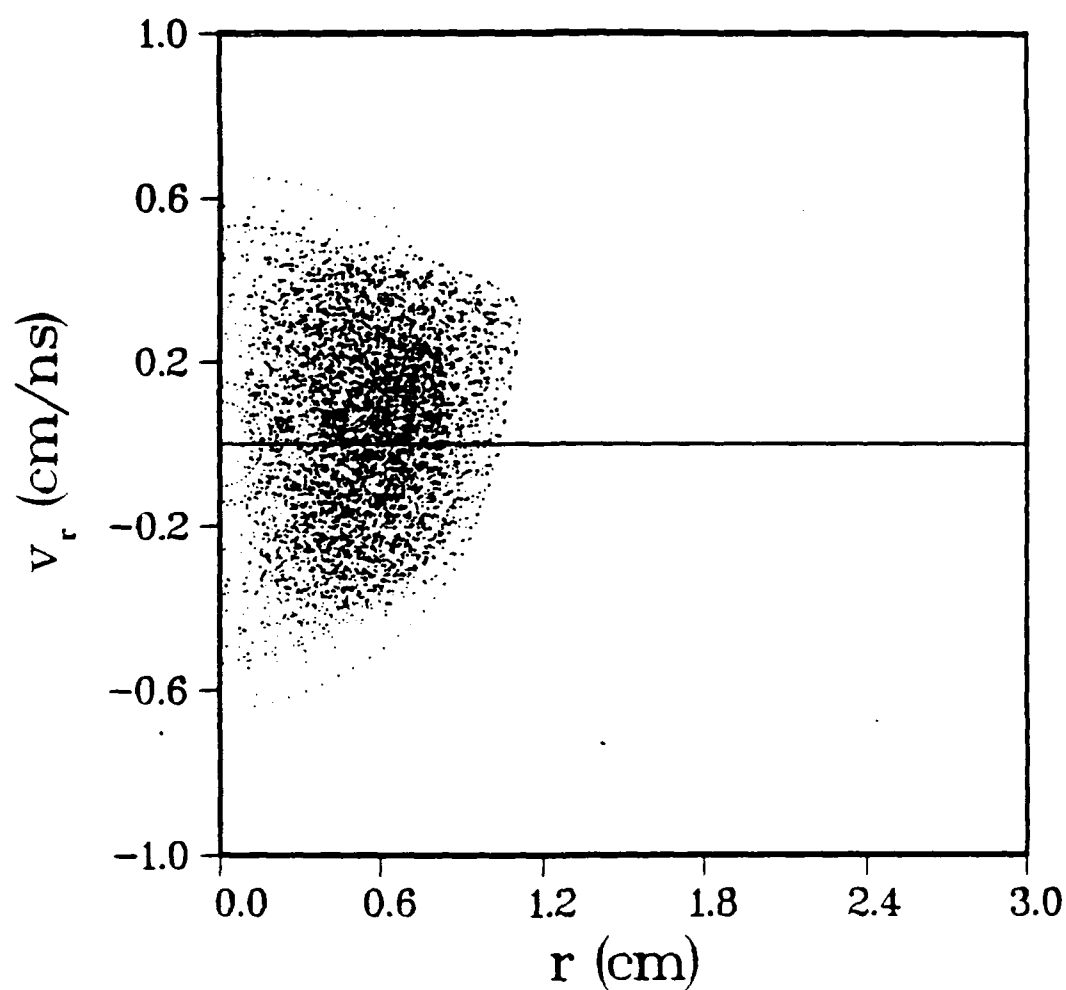


Figure 16 Distribution of ions in the r - v_r plane for the ion beam with initial spread in v_θ comparable to the initial spread in v_r at the theoretical focal plane.

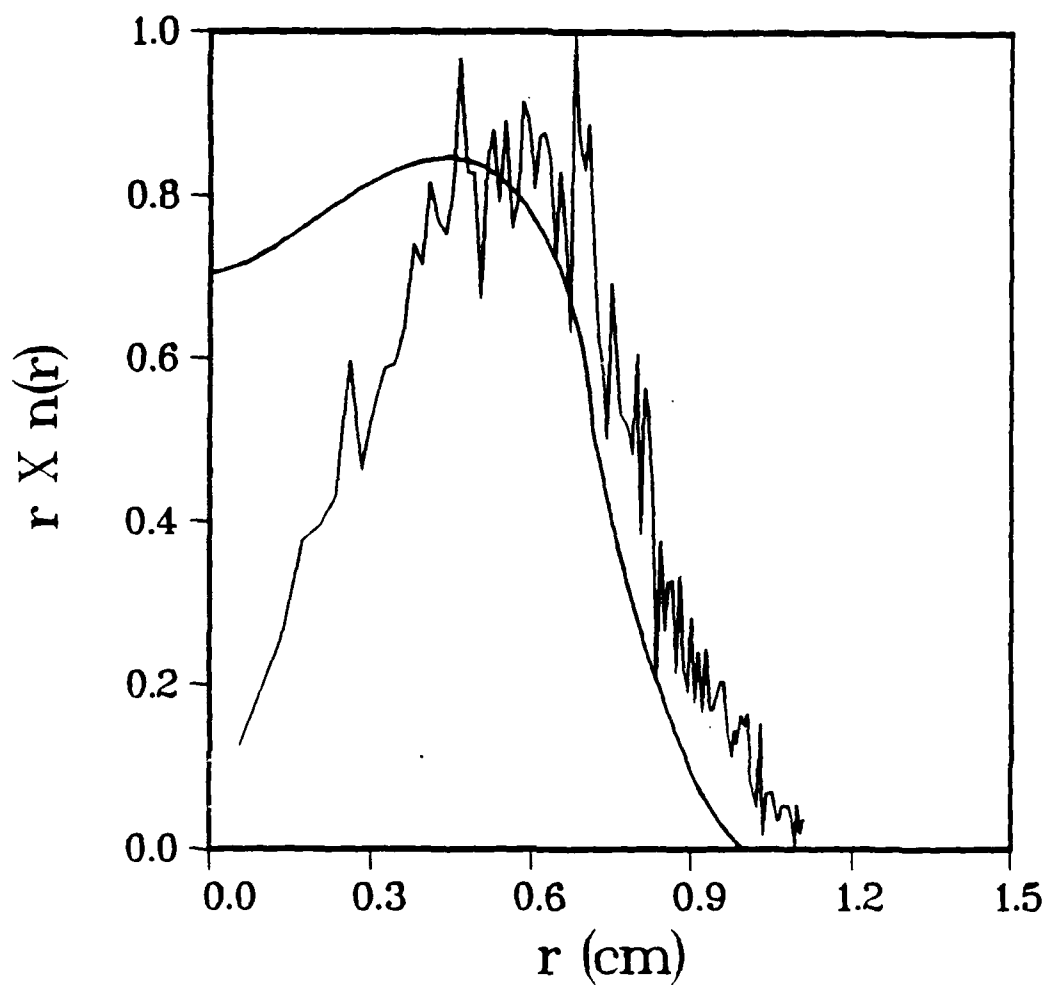


Figure 17 $rn(r)$ profile of the ion beam with initial spread in v_θ comparable to the initial spread in v_r at the theoretical focal plane.

DISTRIBUTION FOR DOE SPONSORED WORK
15 March 1988

U.S. Department of Energy
Office of Inertial Fusion
Washington, DC 20545

Attn: S.L. Kahalas 1 copy
R.L. Schriever 1 copy

U.S. Department of Energy
Office of Classification
Washington, DC 20545

Attn: Robert T. Duff 1 copy

U.S. Department of Energy
Nevada Operations Office
P.O. Box 14100
Las Vegas, NV 89114

2 copies

U.S. Department of Energy
P.O. Box 62
Oak Ridge, TN 37830

1 copy

Cornell University
Ithaca, NY 14850

Attn: D.A. Hammer 1 copy
R.N. Sudan 1 copy

Defense
Technical Information Center Station
Duke Street
Alexandria, VA 22314
Attn: T.C.

2 copies

JAYCOR, Inc.
1608 Spring Hill Rd.
Vienna, VA 22180-2270

Attn: B.V. Weber 1 copy
D.D. Hinshelwood 1 copy

KMS Fusion, Inc.
3941 Research Park Drive
P.O. Box 1567
Ann Arbor, MI 48106
Attn: A.A. Glass

1 copy

Lawrence Berkley Laboratory
Berkley, CA 94720
Attn: D. Keefe

1 copy

Records 1 copy

Director of Research
U.S. Naval Academy
Annapolis, MD 21402

2 copies

Code 1220 1 copy

Code 2634 Cindy Sims 1 copy

Lawrence Livermore National Laboratory
P.O. Box 808
Livermore, CA 94550

Attn: R. Batzel/J. Kahn, L-1 1 copy
J. Emmett, L-488 1 copy
W. Krupke, L-488 1 copy
E. Storm, L-481 1 copy
J. Lindl, L-477 1 copy

Los Alamos Scientific Laboratory
P.O. Box 1663

Los Alamos, NM 87545
Attn: S.D. Rockwood.
ICF Prog. Mgr.
DAD/IF/M/S 527 1 copy

Naval Research Laboratory
4555 Overlook Ave., S.W.
Washington, D.C. 20375-5000

Attn: Code/Name
2628/TID Dist 22 copies
1000/T. Coffey 1 copy
4000/W. Ellis 1 copy
4040/J. Boris 1 copy
4700/S.L. Ossakow 26 copies
4701/I. Vitkovitsky 1 copy
4710/C. Kapetanakis 1 copy
4720/J. Davis 1 copy
4730/S. Bodner 1 copy
4740/W. Manheimer 1 copy
4750/R. Meger 1 copy
4760/B. Robson 1 copy
4770/G. Cooperstein 10 copies
4770.1/F. Young 1 copy
4770.1/D. Mosher 1 copy
4770.2/R. Commisso 1 copy
4771/P. Ottinger 1 copy
4771/J. Neri 1 copy
4771/J. Grossmann 1 copy
4773/S. Stephanakis 1 copy
4790/D. Colombant 1 copy
4790/I. Haber 1 copy
4790/M. Lampe 1 copy
4600/D. Nagel 1 copy

Sandia National Laboratories
P.O. Box 5800

Albuquerque, NM 87185
Attn: J.P. VanDevender/1200 1 copy
D.L. Cook/1250 5 copies
T. Martin/1250 1 copy

University of Rochester
250 East River Road
Rochester, NY 14623
Attn: J. Eastman

1 copy